Heliyon 12 (2026) e45105

Contents lists available at ScienceDirect

Heliyon

journal homepage: www.cell.com/heliyon

Research article

Clay-supported CuO nanoparticles: Synthesis, characterization, and photocatalytic activities for malachite green decolorization

Getu Worku Wudu, Belete Asefa Aragaw, Alebel Nibret Belay *

Department of Chemistry, College of Science, Bahir Dar University, P.O. Box 79, Bahir Dar, Ethiopia

ARTICLE INFO

Keywords:
Photocatalysis
Nanocomposite
Clay
Nanoparticle synthesis
Environmental remediation
Malachite green dye

ABSTRACT

Highly porous, clay-supported nanomaterials have great potential to advance catalysis. In this study, we synthesized a clay-supported copper oxide nanocomposite (CuO NCPs) using the co-precipitation method, specifically designed for the photocatalytic decolorization of malachite green dye (MG). The copper oxide nanoparticles (CuO NPs (**1**)) and clay-supported CuO NCPs (**2**) were characterized using UV-Vis, FTIR, XRD, BET, and SEM-EDX to investigate optical properties, molecular structure, crystal structure, surface area and pore size distribution, surface morphology, and elemental composition. Key quantitative results include: average crystallite sizes of 11.73 nm (CuO NPs) and 11.97 nm (CuO NCPs) by XRD; approximate band gap energies of 2.16 eV and 2.07 eV, respectively. The clay-supported CuO NCPs (**2**) achieved 89.67 ± 1.4% decolorization compared to 82.96 ± 1.8% for unsupported CuO NPs (**1**) under identical conditions, a modest but statistically significant improvement ($p = 0.012$) after 180 min under a 200 W tungsten lamp. Adsorption during dark equilibration accounted for 9.8% and 11.3% of total removal, respectively, confirming that photochemical processes dominate. We report decolorization (loss of chromophore) rather than complete mineralization; TOC analysis was not performed. Raw smectite clay exhibits a moderate BET surface area of 73.67 m^2/g with a total pore volume of 0.156 cc/g and an average pore diameter of 8.47 nm, characteristic of mesoporous 2:1 layered aluminosilicates with interlayer and interparticle voids. Upon synthesis of unsupported CuO NPs (1), a significant reduction in surface area to 27.05 m^2/g was observed, accompanied by a decrease in pore volume to 0.094 cc/g and an increase in average pore diameter to 13.90 nm. Notably, the clay-supported CuO NCPs (2) recovered a substantially higher surface area of 36.14 m^2/g and pore volume of 0.132 cc/g compared to unsupported CuO, while maintaining a large average pore diameter of 14.61 nm. We acknowledge the absence of reusability studies and scavenger tests as limitations of this study. Overall, composite materials combining adsorption and photocatalysis exhibit promising properties for removing hazardous dyes from wastewater, as the clay support improves CuO NPs dispersion and increases accessible surface area. However, further optimization, mineralization studies (TOC/COD), and mechanistic studies are required before industrial application.

1. Introduction

According to the World Water Development Report 2025, approximately 2.2 billion people lack access to safely managed drinking

* Corresponding author.
E-mail addresses: getuworku2112@gmail.com (G.W. Wudu), beliyeeed@gmail.com (B.A. Aragaw), alebel.nibret@bdu.edu.et (A.N. Belay).

https://doi.org/10.1016/j.heliyon.2026.e45105
Received 9 December 2025; Received in revised form 10 June 2026; Accepted 11 June 2026
Available online 17 June 2026

water, with industrial pollution from textile effluents being a major contributor in developing countries. The global textile industry produces an estimated 280,000 tons of synthetic dyes annually, of which 10-15% are released into wastewater without adequate treatment [1]. The relentless pace of global industrialization, particularly within the textile, leather, and aquaculture sectors, has led to a steady increase in the discharge of hazardous synthetic dyes into aquatic ecosystems [2,3]. Among these, malachite green (MG), a cationic triphenylmethane dye, is of particular concern. While it has been used globally as an industrial colorant and an effective antifungal and antiparasitic agent in aquaculture, substantial evidence has unequivocally linked MG to severe health risks, including carcinogenicity, teratogenicity, and mutagenicity in aquatic life and humans [4,5]. Even at low concentrations (mg/L levels), MG poses a significant threat, interfering with photosynthesis in aquatic plants, obstructing sunlight penetration, and accumulating in the fatty tissues of organisms where it metabolizes into the more persistent leuco-malachite green (LMG) [6]. Consequently, MG has been banned or strictly regulated in many countries, yet it remains a pervasive pollutant in industrial effluents due to its low cost and continued illicit use, necessitating urgent and effective remediation strategies.

Traditional wastewater treatment methods, such as membrane filtration, coagulation, and biological treatments, often fall short when applied to MG. These methods can be costly, energy-intensive, or inefficient, frequently leading to secondary pollution or merely transferring the contaminant to another phase rather than destroying it [7,8]. In response, semiconductor-based heterogeneous photocatalysis has emerged as a superior, sustainable, and cost-effective advanced oxidation process (AOP). This technology leverages solar or artificial light to generate reactive oxygen species (ROS) that can mineralize complex organic pollutants like MG into harmless byproducts such as carbon dioxide (CO_2) and water (H_2O) [9,10]. In the search for efficient photocatalysts, copper oxide (CuO) has garnered significant attention. As a narrow band gap (1.2–1.5 eV) p-type semiconductor, CuO is capable of harvesting a broad spectrum of visible light, which constitutes a major portion of solar radiation [11,12]. Recent advances in 2024 and 2025 have demonstrated the remarkable potential of CuO-based systems. For instance, a novel dual Z-scheme CuO/BCN/MXene heterojunction was engineered to achieve 98.3% degradation of MG, attributed to its tailored band alignment that dramatically improves charge carrier separation [13,14]. Similarly, a green-synthesized $LaCeO_3$/CuO nanocomposite achieved 92.88% MG degradation within 120 min, showcasing the synergy of combining CuO with other metal oxides [15]. Ionic liquid-coated metaloxide nanoparticles have also exhibited enhanced photodegradation efficacy compared to their bare counterparts [16]. Despite these advancements, the practical application of bare CuO nanoparticles is often hindered by several intrinsic drawbacks. Their high surface energy leads to severe aggregation, which reduces the number of available active sites. Furthermore, the rapid recombination rate of photo-generated electron-hole pairs significantly limits their quantum efficiency and overall photocatalytic performance [10,17]. To overcome these limitations, a widely adopted strategy involves dispersing and stabilizing CuO nanoparticles onto robust, high-surface-area support materials. Among various supports, natural clay minerals, particularly smectites like montmorillonite, are exceptionally promising. Clays offer unique advantages: they are naturally abundant, low-cost, and possess a layered structure with high specific surface area, excellent adsorption capacity, and favorable cation-exchange properties [18,19]. The clay matrix serves a dual role: it acts as a physical barrier to prevent CuO nanoparticle agglomeration and enhances the adsorption of dye molecules, concentrating them near the photocatalytic active sites [20]. Recent literature from 2024 to 2025 strongly supports the clay-supported approach. Chagour et al. (2025) demonstrated that monometallic catalysts supported on clay exhibit superior MG removal due to synergistic adsorption and photocatalysis [21]. Fatimah et al. (2022) extensively reviewed the role of clay-supported metal oxides in catalytic AOPs, highlighting their enhanced stability and activity [12]. Furthermore, Asamoah et al. (2020) confirmed that clay-nanocomposites significantly outperform their individual components in water purification applications [22]. This synergistic combination of adsorption and photocatalysis not only enhances pollutant removal efficiency but also improves the longevity and reusability of the catalyst.

In this study, we build upon these cutting-edge advancements to develop a novel, cost-effective, and sustainable clay-supported CuO nanocomposite (CuO NCPs (**2**)). Using a simple co-precipitation method, we anchored CuO NPs (**1**) onto a natural smectite clay matrix sourced from Ethiopia. The synthesized materials were rigorously characterized to analyze their structural, optical, and morphological properties. We then systematically evaluated the photocatalytic performance of the nanocomposite for the decolorization of MG under visible light (tungsten bulb) irradiation. We hypothesize that the intimate interaction between the CuO NPs and the clay support will ensure a more uniform dispersion of the nanoparticles and reduce agglomeration, thereby increasing the number of accessible active sites for dye adsorption and photocatalytic reaction. The objective is to demonstrate that the clay-supported CuO NCPs (**2**) exhibit superior photocatalytic efficiency, stability, and reusability compared to unsupported CuO NPs (**1**), offering a promising and scalable solution for the remediation of MG-contaminated wastewater from textile and aquaculture industries. In general, In this study, the selection of smectite clay as the support material for CuO NPs was based on four key considerations: (i) smectite's high specific surface area (typically 200–800 m^2/g) provides abundant sites for CuO nanoparticle deposition and dye adsorption; (ii) its cation exchange capacity (80–150 meq/100g) enables efficient ion exchange for metal precursor loading; (iii) its 2:1 layered structure (tetrahedral-octahedral-tetrahedral, TOT) offers excellent chemical and thermal stability during calcination at 450 °C; and (iv) its natural abundance in Ethiopia, particularly in the Awi zone near the Abay River, makes it a locally available, low-cost alternative to synthetic supports like graphene or carbon nanotubes. The weight ratio of CuO to clay was optimized based on preliminary experiments to maximize photocatalytic activity while maintaining structural integrity; higher CuO loadings led to nanoparticle agglomeration, while lower loadings resulted in insufficient active sites for efficient dye decolorization. While clay-supported CuO systems have been reported in the literature [23], significant gaps remain: (i) most studies use commercially purified clays rather than locally sourced natural clays; (ii) systematic comparison of unsupported versus clay-supported CuO under identical conditions is lacking; (iii) the specific performance of Ethiopian smectite clay for this application has not been reported; and (iv) the distinction between adsorption and photocatalytic decolorization is often blurred. This study addresses these gaps by synthesizing and characterizing clay-supported CuO NCPs using locally sourced Ethiopian smectite clay and comparing their decolorization efficiency with unsupported CuO NPs under controlled conditions. In this context, *decolorization* of MG is defined as the loss of

the characteristic green color due to the destruction of the chromophore. While complete mineralization to CO_2 and H_2O is the ultimate goal of photocatalysis, decolorization provides a rapid, cost-effective screening metric for photocatalytic activity and is widely used in the literature [24,25]. Therefore, this study focuses on the synthesis and characterization of CuO NPs (1) and clay-supported CuO NCPs (2) through a co-precipitation process for the decolorization of MG, a common dye in industrial effluents. By leveraging the synergistic properties of CuO and clay, this research aims to improve photocatalytic performance and offer a sustainable solution for dye removal from wastewater. The enhanced stability and catalytic activity of these nanocomposites hold potential for broader applications in energy storage, environmental remediation, and catalysis [26,27].

2. Experimental section

2.1. Sample site

A clay soil sample was collected from the Amhara region of northern Ethiopia, specifically from the Awi zone in Ligaba Kebele, located near the Abay River (Blue Nile). The sampling site is approximately 20 km from Dangla town, 68 km northwest of Bahir Dar city, and 500 km northwest of Addis Ababa. The sample was extracted at a depth of 3.5 m below the surface using a hand drill, sealed in a polyethylene bag, and stored under dry, cool conditions at the Bahir Dar University laboratory for further experimental analysis [20]. Smectite, a widely used clay in catalytic applications, was identified as the primary clay type for supporting metal and metal oxide catalysts, particularly in advanced oxidation processes (AOPs) and specific catalyzed organic reactions. Smectite is a 2:1 layered clay mineral, also referred to as Tetrahedral-Octahedral-Tetrahedral (T-O-T) in its crystal structure. It belongs to the hydroxyl alumino-silicate family and is composed of two tetrahedral silica layers sandwiching one octahedral alumina layer. Naturally occurring smectites, such as montmorillonite, saponite, beidellite, nontronite, and hectorite, form through the weathering of soils or volcanic ash. These smectites exhibit variable chemical compositions, with Fe^{2+}, Mg^{2+}, or Mn^{2+} often replacing Al^{3+} in the octahedral positions and Al^{3+} or Fe^{3+} substituting Si^{4+} in the tetrahedral sites [18]. Smectites are particularly notable for their high swelling capacity, which results from their ability to hydrate easily and their elevated cation-exchange capacity. Their large surface area, derived from their thin, layered structure and small particle size, facilitates the absorption of various substances, including organic molecules, making them valuable in catalysis and other industrial processes [28,29].

2.2. Materials

All chemicals utilized in the synthesis were commercially obtained and of analytical reagent grade, and were employed without additional purification. The materials included $CuSO_4{\cdot}5H_2O$ (98%, Sigma-Aldrich, USA), C_2H_5OH (99.5%, Himedia, India), NaOH (98%, Merck, Germany), and HCl (37%, Sigma-Aldrich, USA). In contrast, the clay supporting material was collected from Ligaba Kebele, Awi zone, Amhara region, Ethiopia. The experiment was conducted using distilled water (prepared in the laboratory, with a resistivity of 18.2 MΩ cm, using an Aqua Solutions water purification system) for solution preparation. All glassware was cleaned with aqua regia (3:1 HCl: HNO_3) and rinsed thoroughly with deionized water before use to prevent contamination.

2.3. Synthesis of CuO NCPs (1)

CuO NPs (1) were synthesized following the procedure outlined in our previous work [30]. A 0.2 M solution of $CuSO_4{\cdot}5H_2O$ (3.5 g) was prepared and added to a 250 mL Erlenmeyer flask containing 70 mL of ethanol. The mixture was then heated to 70 °C with continuous stirring. To this solution, 0.2 M NaOH (0.56 g) was introduced dropwise while monitoring the pH, which was adjusted to 12, accompanied by a color change from green to black. The appearance of the black color indicated the formation of amorphous $Cu(OH)_2$ [31]. The resulting dark residue was filtered and washed several times with deionized water to remove sulfate ions, followed by centrifugation at 4000 rpm for 15 min. The product was then dried in an oven at 70 °C for 12 h and subsequently calcined at 450 °C for 4 h. The final product, designated as CuO NPs (**1**), was stored for future characterization.

$$CuSO_4.5H_2O + 2NaOH \rightarrow Na_2SO_4 + Cu(OH)_2 \quad (1)$$

$$Cu(OH)_2 + Heat \rightarrow CuO + H_2O \uparrow \quad (2)$$

2.4. Synthesis of clay-supported CuO nanocomposites (2)

The distribution of metal oxide nanoparticles on the natural clay structure can be achieved through an ion exchange process, where metal ions replace the native cations of the clay mineral, or by directly dispersing the metal oxide nanoparticles in situ within the clay matrix. Clay-supported CuO NCPs were prepared using a slightly modified procedure [32,33]. The dried natural clay was first ground into a fine powder using a mortar and pestle. A 10 g sample of the ground clay was then dispersed in 1000 mL of distilled water to form a clay suspension with a concentration of 10 g/L. The mixture was shaken at 150 rpm for 72 h at room temperature to ensure complete dispersion of the clay particles. The suspension was then allowed to settle, and the supernatant was decanted. The clay was washed several times with distilled water to remove impurities. The wet clay was subsequently dried in an oven at 100 °C for 12 h, followed by sieving through a 250 μm mesh to ensure uniform texture and homogeneity. The treated clay was stored in tightly sealed polyethylene bags, labeled as clay sample A, and kept in a cool, dry place until further use. To prepare the clay-supported CuO NCPs, 30 mL of the

clay suspension from sample A was added to a solution containing 0.2 M $CuSO_4{\cdot}5H_2O$ (4.994 g). Based on the initial 10 g/L clay concentration, the 30 mL aliquot provided 0.3 g of clay; this was combined with 4.994 g of $CuSO_4{\cdot}5H_2O$ (equivalent to approximately 1.27 g of CuO after complete conversion), giving a theoretical CuO-to-clay mass ratio of roughly 1:10. NaOH was then added dropwise to adjust the pH to 10.7 under continuous stirring. The reaction mixture was heated to 70 °C and maintained for 24 h. After cooling, the dark brown residue was washed several times with deionized water to remove residual sulfate ions and centrifuged at 4000 rpm for 15 min. The final product was dried in an oven at 80 °C for 12 h and then calcined at 450 °C for 4 h. The resulting material was designated as clay-supported CuO NCPs (**2**) (Fig. 1).

2.5. Photocatalytic decolorization studies

The catalytic performance of the synthesized CuO NPs (**1**) and clay-supported CuO NCPs (**2**) was evaluated for the decolorization of MG. The photocatalytic experiments were conducted using a tungsten fluorescent lamp as the light source, with both photocatalysts (**1**) and (**2**) tested under identical conditions. The photocatalytic decolorization experiments were conducted in a custom photoreactor consisting of a cardboard box lined with aluminium foil (internal dimensions: 30 × 30 × 40 cm) to maximize light reflection and minimize external interference. A 250 mL borosilicate glass beaker served as the reaction vessel, containing a mixture of 0.0492 g of photocatalyst powder and 150 mL of 20 ppm malachite green (MG) aqueous solution. The suspension was continuously stirred at 3000 rpm using a magnetic stirrer to ensure uniform catalyst dispersion and mass transfer. Before irradiation, the reaction mixture was stirred in the dark for 30 min to establish adsorption-desorption equilibrium. During this dark period, 5 mL aliquots were withdrawn every 5 min (at t = 5, 10, 15, 20, 25, and 30 min) to monitor the adsorption kinetics. After the dark equilibration period, the tungsten lamp (200 W) was switched on to initiate photocatalysis. Thereafter, 5 mL aliquots were withdrawn every 30 min (at t = 30, 60, 90, 120, 150, and 180 min of illumination). Heat generated by the lamp was carefully managed; the reaction temperature was monitored throughout and maintained at 32 ± 2 °C. At 30-min intervals. All aliquots were centrifuged at 3000 rpm for 5 min, filtered to remove catalyst particles, and analyzed. The aliquots were discarded after analysis and not returned to the reaction vessel. The reduction in reaction volume was accounted for in the decolorization calculations using equations (2.3) and (2.4). The light source was a tungsten fluorescent lamp (Philips Tornado, 200 W, 220 V, 0.18 A, 50 Hz) positioned 9 cm above the reaction vessel, delivering a measured irradiance of 8.26 mW/cm^2 over an illuminated area of approximately 50 cm^2 at the solution surface. According to the manufacturer's specifications and confirmed by preliminary measurements with a USB4000 spectrometer (Ocean Optics), the lamp emits over a broad spectral range of 350–800 nm, with a maximum intensity around 650 nm (visible region). The ultraviolet contribution (300–400 nm) is minimal, accounting for less than 5% of the total integrated intensity, while the infrared portion (>700 nm) constitutes approximately 30%, contributing primarily to heat generation. No optical filters were employed, so the reaction system was exposed to the full emission spectrum of the lamp. The tungsten lamp was selected due to its broad visible-light emission suitable for simulating solar-driven photocatalysis, its affordability and availability in Ethiopia, its low UV output enabling emphasis on visible-light activity, and its prior application in similar studies [34,35]. The absorbance of the MG solution was then measured at its maximum absorption wavelength (617 nm), with the pH maintained at 7. A notable limitation of the tungsten lamp is its significant heat generation; however, this was carefully monitored as summarized in Table 8 (Section 3.8). The percentage of MG decolorization was calculated using Eq. (3) [36].

$$\text{Removal percentage } \% = \frac{Co - Ct}{Co} \times 100 \tag{3}$$

In the equation above, *C*o denotes the initial dye concentration, while *C*t represents the concentration at time *t*. Furthermore, the rate of dye decolorization at a specific time *t* was determined using Eq. (4) [37].

$$ln\frac{Ct}{Co} = -\kappa t \tag{4}$$

Fig. 1. Synthesis path of clay-supported CuO NCPs (**2**).

2.6. Characterization techniques

This study was conducted at the College of Natural Sciences, Department of Chemistry, Bahir Dar University, Ethiopia. The synthesized CuO NPs (**1**) and clay-supported CuO NCPs (**2**) were characterized using UV-Vis spectroscopy (DU-8800D spectrophotometer, optical system: Double Beam, Blazed Holographic Grating (1200 lines/mm), China) and FT-IR spectroscopy (FT/IR-6600 FTIR Spectrometer, JASCO, USA). Scanning electron microscopy, combined with energy-dispersive X-ray spectroscopy (SEM-EDX), was employed using a HITACHI S4700 microscope with Quantax (China) for morphological analysis. X-ray diffraction (XRD) measurements were performed using a BRUKER D8 Advance XRD system (Germany), equipped with a Cu target for generating Cu Kα radiation (wavelength 1.5406 Å). The XRD analysis was conducted at Addis Ababa University, Ethiopia. Brunauer-Emmett-Teller (BET) analysis was conducted at Bahir Dar Institute of Technology, Bahir Dar, Ethiopia, to provide further information on the surface area and pore size distribution of raw clay, and the photocatalyst was analyzed by the BJH model. For UV-Vis characterization, 1 mg of each synthesized photocatalyst (**1**) and (**2**) was dispersed in 10 mL of a mixed solvent of DMF/ethanol (1:2 v/v) and sonicated using a Sonar-made (40 kHz) ultrasonicator to obtain a stable suspension for optical absorption measurement (see Fig. 1).

3. Results and discussion

3.1. UV-visible spectra analysis

The ultraviolet-visible (UV-Vis) absorption spectra for clay (**a**), the synthesized photocatalysts (**1**) (**b**), and (**2**) (**c**) are presented in Fig. 2 and Table 1. Both CuO NPs (**1**) and clay-supported CuO NCPs (**2**) exhibit light absorption in the ultraviolet region. The spectra reveal characteristic deep-UV absorption peaks at 264 nm for clay (a), 222 nm for photocatalyst (2) (b), and 226 nm for photocatalyst (1) (c), corresponding to their respective electronic transitions. Whereas the band-to-band transitions and defect-related transitions were observed as a broad peak at 485 nm for clay (**a**), 573 nm for CuO NPs (**1**) (**b**), and 598 nm for clay-supported CuO NCPs (**2**) (**c**), which is related to the electronic transition from the valence to the conduction band [38,39]. Notably, a red shift was observed in the NCPs (**2**) (**c**) compared to clay (**a**), which may be attributed to the synergistic effect of the higher concentration of CuO in the clay-supported CuO NCPs (see Tables 4 and 5). The broad absorption band observed in the visible region (485–598 nm) is attributed to a combination of band-to-band electronic transitions and defect-related states, such as oxygen vacancies and copper interstitials [38]. This absorption originates from transitions between the valence and conduction bands, as well as from localized states within the band gap. The optical behavior is influenced by nanoparticle size, which affects the electronic structure and, consequently, light–matter interactions. Additionally, the surrounding chemical environment, including the solvent, can modify the optical properties of both CuO nanoparticles (1) and clay-supported CuO nanocomposites (2). These effects are characteristic of nanoscale materials, where variations in size and environment lead to changes in absorption behavior [40].

Furthermore, the broad and featureless UV–Vis absorption spectra observed for both CuO NPs (**1**) and clay-supported NCPs (**2**) are characteristic of such systems and do not imply unsuccessful synthesis. This behavior is mainly attributed to small particle size and size distribution (polydispersity), which lead to overlapping absorption bands, as well as surface defects and lattice strain that introduce localized states and extend absorption into the visible region (Figs. 3 and 4). In addition, nanoparticle agglomeration enhances light scattering, further smoothing spectral features. For NCPs, the clay support contributes additional scattering and interfacial interactions with CuO, which can shift and broaden the absorption edge. The predominantly indirect bandgap nature of CuO NPs, along with possible minor contributions from Cu_2O phases, results in a gradual, poorly defined absorption profile. Therefore, complementary techniques such as XRD, BET, FTIR, and SEM-EDX were essential to confirm phase composition and structural characteristics

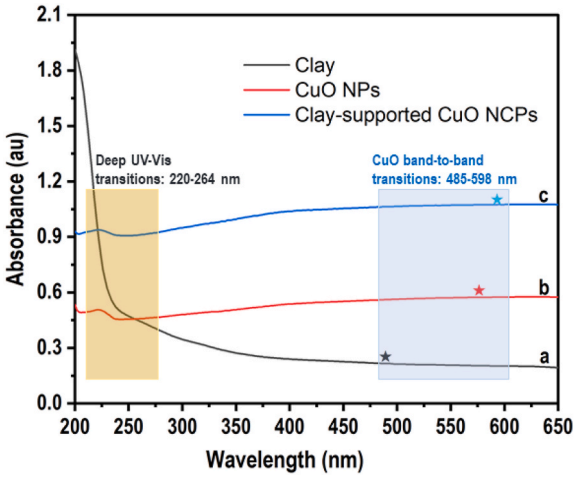

Fig. 2. UV-Visible spectra of the CuO NPs (**1**) (0.001 M) and clay-supported CuO NCPs (**2**) (0.001 M), at 25 °C with a mixed solvent of DMF/ethanol (1:2).

Table 1
Absorbance, maximum wavelengths, and band gaps of CuO NPs (**1**) and clay-supported CuO NCPs (**2**).

Compounds	Absorbance	Maximum-wavelength (nm)	Band gap (Eg) (eV)
CuO NPs (**1**)	0.51	573	2.16
Clay-supported CuO NCPs (**2**)	0.94	598	2.07

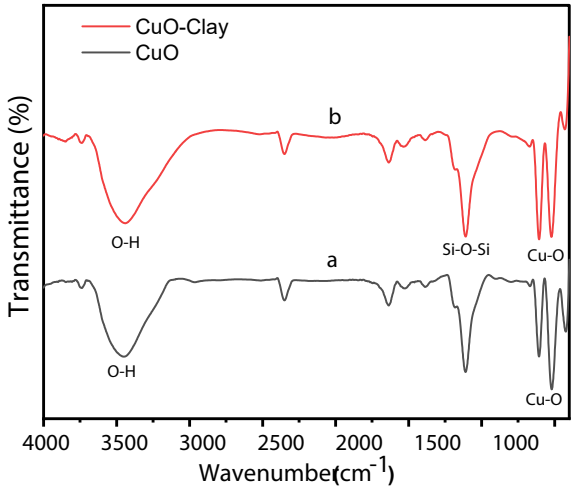

Fig. 3. FTIR spectra of a) CuO NPs (**1**) (black) and b) Clay-supported CuO NCPs (**2**) (red).

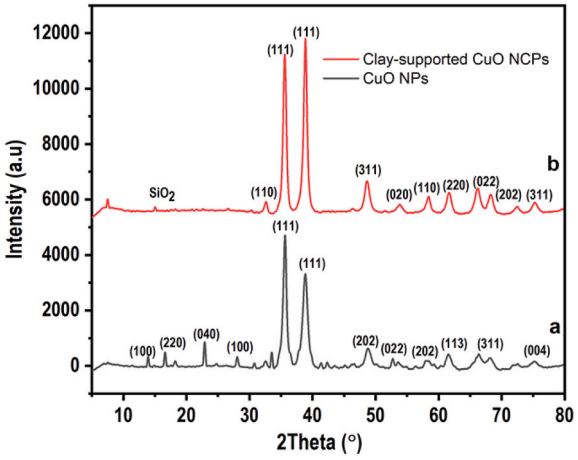

Fig. 4. The XRD diffractograms of as-synthesized photocatalysts (**1**)(a) (black) and (**2**)(b)(red) NCPs.

(Figs. 3–7).

The band gap energy (Eg) of CuO NPs (**1**) and clay-supported CuO NCPs (**2**) were calculated using the equation depicted below [30]:

$$E_g = \frac{1240eV}{\lambda} \quad (5)$$

Where Eg is the band gap energy in electron volts, and λ is the wavelength (nm) corresponding to the absorption edge. The optical band gap of CuO is significantly affected by its size. In its bulk form, CuO has a typical band gap of 1.2-1.5 eV, while synthesized CuO NPs can exhibit band gap energies from 1.5 eV up to 3.5 eV due to quantum confinement effects and surface interactions [11,38]. The observed Eg values (2.16 eV for CuO NPs and 2.07 eV for clay-supported CuO NCPs) fall within this range for nanocrystalline CuO. The slightly lower band gap of the clay-supported sample compared to unsupported CuO may be attributed to interfacial interactions between CuO and the clay matrix, which can modify the electronic structure. Importantly, these values represent apparent optical band gaps derived from the absorption edge using the simplified Tauc plot method (Eg = 1240/λ). This approach assumes direct allowed transitions and

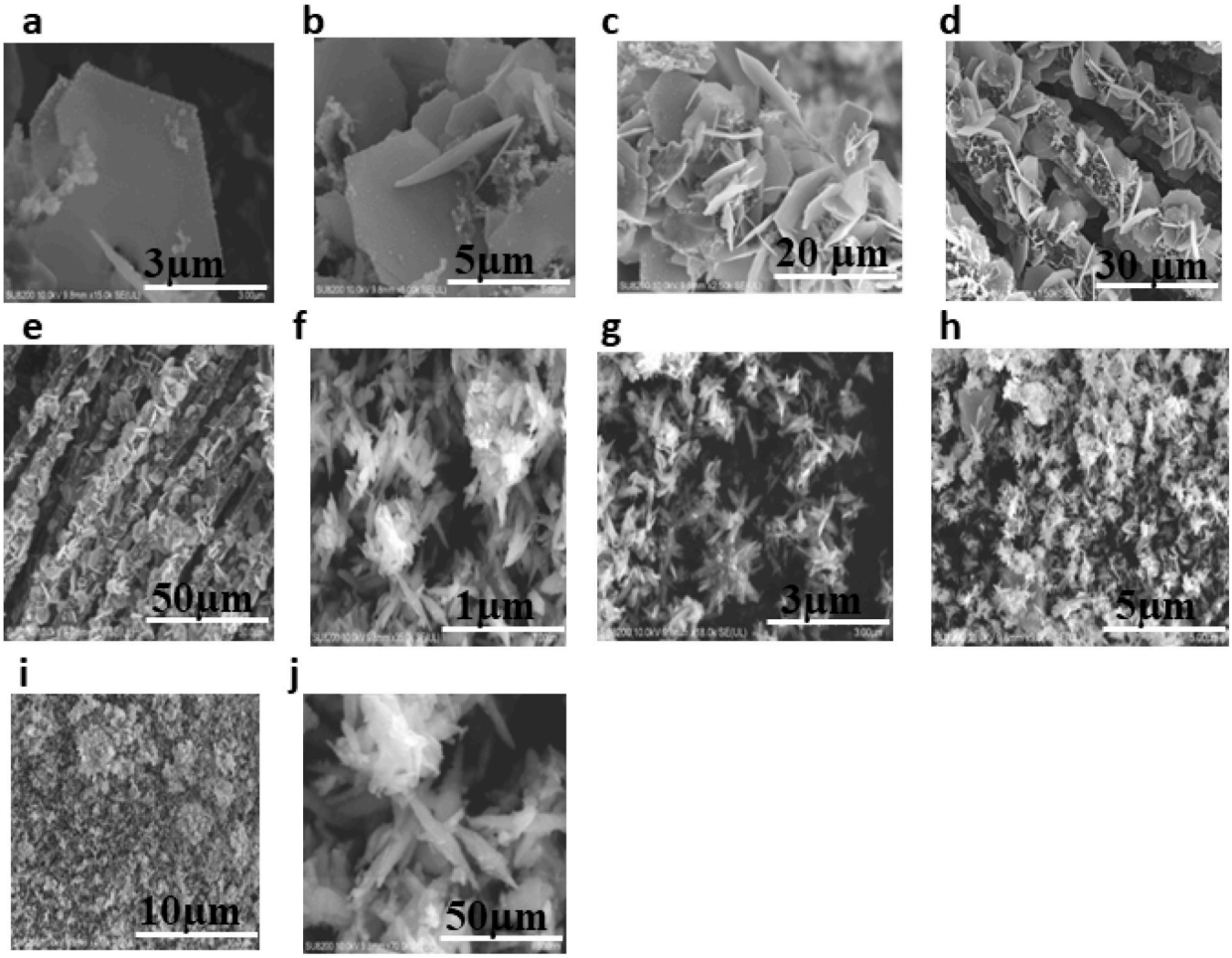

Fig. 5. SEM image of the synthesized photocatalysts (**1**) (a-e) and (**2**) (f-j) in different size ranges (1-50 μm).

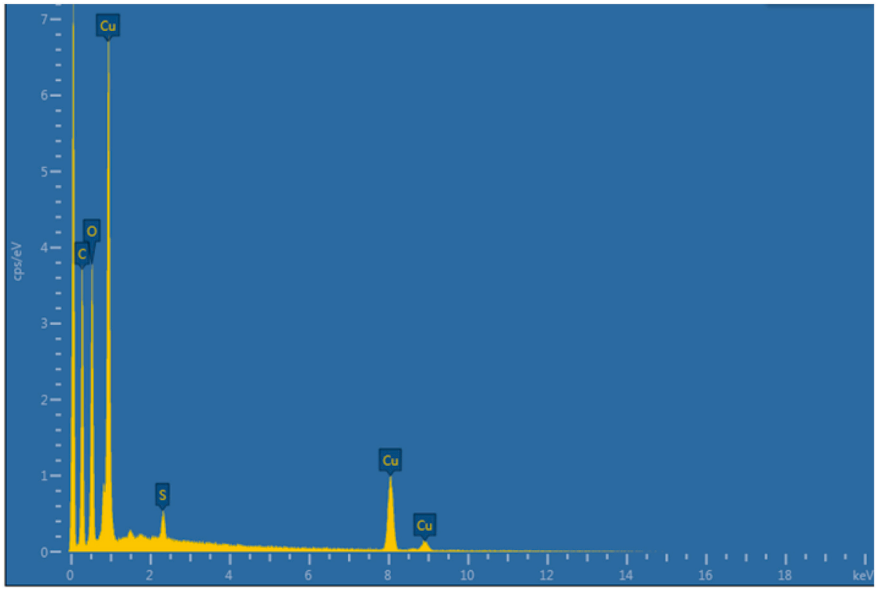

Fig. 6. EDX spectrum of CuO NPs (**1**).

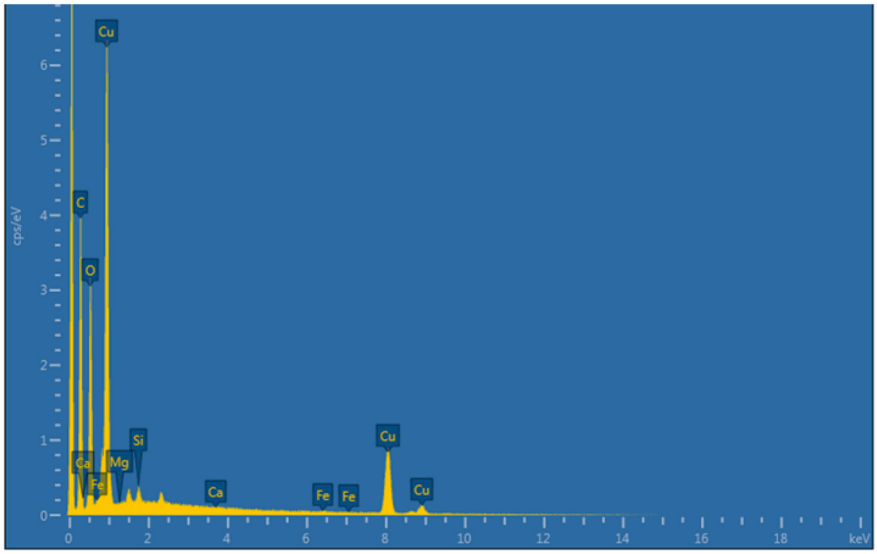

Fig. 7. EDX spectrum of clay-supported CuO NPs (**2**).

does not distinguish between direct and indirect band gap behavior. CuO is known to exhibit predominantly indirect transitions, and a more rigorous Tauc plot analysis (absorbance vs. photon energy with appropriate power exponents) would be required for precise band gap determination. Additionally, defect-related absorption tails (Urbach tails) arising from oxygen vacancies, copper interstitials, and lattice strain contribute to the broad absorption observed in the visible region (485-598 nm). The Urbach energy (Eu), which quantifies disorder-induced band tailing, can be estimated from the exponential absorption edge; however, such analysis requires high-resolution absorption data near the band edge that were not collected in this study. Therefore, the reported Eg values should be considered as approximate indicators of optical behavior rather than definitive electronic parameters.

3.2. The FTIR spectra analysis

The FTIR spectra, shown in Fig. 3, were recorded in the range of 400-4000 cm^{-1} for both CuO NPs (**1**)(a) and clay-supported CuO NCPs (**2**)(b). The FTIR analysis clearly confirms the successful formation of both CuO NPs (**1**) and clay-supported CuO NCPs (**2**), while also highlighting key structural differences arising from the clay matrix. For pristine CuO NPs, the characteristic peaks at ~516–606 cm^{-1} are assigned to Cu–O stretching vibrations of the monoclinic phase, accompanied by peaks at ~1638 and 3454 cm^{-1} corresponding to adsorbed water (H–O–H bending and O–H stretching), and weak features near ~2930 cm^{-1} attributed to residual organic species from synthesis. In contrast, the clay-supported CuO NCPs exhibit additional distinct peaks, particularly at ~1043 cm^{-1} (Si–O–Si/Si–O–Al stretching), confirming the presence of layered aluminosilicate structures such as montmorillonite, alongside Cu–O peaks at ~509 and 605 cm^{-1}. The enhanced intensity and broadening of the O–H stretching (~3454 cm^{-1}) and H–O–H bending (~1632 cm^{-1}) peaks in the composite indicate increased surface hydroxylation and interlayer water retention due to the hydrophilic clay matrix. These findings suggest strong interfacial interactions between CuO and the clay support, which can improve nanoparticle dispersion, reduce agglomeration, and introduce additional active sites compared to bare CuO NPs. Recent studies report similar FTIR features and conclude that clay-supported CuO systems exhibit superior structural stability and surface functionality, leading to enhanced catalytic and adsorption performance relative to unsupported CuO nanoparticles [41,42]. Overall, for pristine CuO NPs (Fig. 3a, black spectrum), the characteristic peaks at ~516-606 cm^{-1} are assigned to Cu-O stretching vibrations of the monoclinic phase. A very weak feature near 1043 cm^{-1} is occasionally observed, which may arise from trace silicate contamination (e.g., from glassware or commercial ethanol stabilizers) or baseline artifacts; importantly, this feature is substantially weaker than the corresponding Si-O-Si/Si-O-Al peak in the clay-supported composite (Fig. 3b, red spectrum), confirming that the unsupported CuO sample is not significantly contaminated by clay. The peaks at ~1638 and 3454 cm^{-1} correspond to adsorbed water (H-O-H bending and O-H stretching), with weak features near ~2930 cm^{-1} attributed to residual organic species from synthesis. The incorporation of clay into the CuO NCPs (**2**)(b)) has a relatively minor impact on the positions and intensities of the FTIR peaks, but it does influence the vibrational modes of the functional groups present in the CuO NPs (**1**)(a)). The interaction between the clay and CuO particles leads to small shifts in certain FTIR peaks, particularly those corresponding to hydroxyl (-OH) groups and Cu-O bonds. These shifts are likely due to alterations in the bonding or hydrogen bonding interactions between the clay and CuO. Moreover, the stretching vibrations of Si–O bonds in the clay component may cause new peaks to appear or result in shifts in the Si–O region of the spectrum. These changes in peak intensity may indicate variations in the number of active sites available for catalysis or reflect modifications in the structural arrangement of CuO within the clay matrix [12].

3.3. X-ray diffraction analysis

The XRD diffractograms of CuO NPs (**1**) and clay-supported CuO NCPs (2) are presented in Fig. 4. The diffraction peaks at 2θ values of CuO NPs (**1**) occur at 14.02°, 16.61°, 22.89°, 28.14°, 35.61°, 38.83°, 48.83°, 52.74°, 58.38°, 61.57°, 66.25°, and 75.42°, corresponding to reflections from the (100), (220), (040), (100), (111), (111), (202), (022), (202), (113), (331), and (004) planes (Fig. 4a). While clay-supported CuO NCPs (**2**), the peaks appear at 32.45°, 35.59°, 38.86°, 48.65°,53.83°, 58.36°, 61.64°, 66.19°, 68.23°, and 75.36° corresponding to the (110), (111), (111), (311), (020), (110), (220), (022), (202), and (331) crystal planes of monoclinic CuO, respectively, which are in good agreement with JCPDS card No. 48-1548 [21,38]. The sharp and intense peaks indicate good crystallinity of both samples. For clay-supported CuO NCPs (**2**), additional small peaks in the 5–30° 2θ range, specifically at approximately 6.8° and 14.5°, correspond to the basal spacing of smectite clay (d_{001} and d_{002} reflections), consistent with JCPDS card No. 13-0135 [21]. These peaks are absent in the unsupported CuO NPs (1) pattern, confirming successful incorporation of the clay support. The absence of other distinct diffraction peaks from the clay in the 10–30° range is attributed to the relatively low clay content and its partially disordered structure. The reduced intensity of CuO peaks in the composite (2) compared to pure CuO is attributed to the dilution effect of the clay matrix and potential partial coverage of CuO by clay layers [43]. Moreover, no visible peak was observed in Fig. 4b within the XRD pattern, covering the diffraction angle range of 10°–30°, which provides strong evidence for the presence of an amorphous SiO_2 shell surrounding the CuO core. However, the presence of the SiO_2 shell does not significantly impact the crystallinity of the CuO NCPs (**2**). The prominent diffraction peaks observed at 35.61° for CuO NPs (**1**) and 38.86° for clay-supported CuO NCPs (**2**) indicate that both materials exhibit a preferred (111) crystal orientation, suggesting the formation of Cu-O bonds in the nanocomposites. The sharpness and intensity of these peaks reflect the well-defined crystalline structure of both materials. The average crystallite sizes for the photocatalysts (1) and (2) were calculated using the Debye-Scherrer equation (Eq. (6)) [44], based on the most intense diffraction peaks corresponding to the (111) crystal planes. The calculated values (11.73 nm for CuO NPs and 11.97 nm for clay-supported CuO NCPs) are within the typical range for nanocrystalline CuO prepared by co-precipitation [39,45]. The similarity in crystallite sizes suggests that the clay support does not significantly alter the primary crystallite growth, consistent with observations by Chagour et al. [21] for clay-supported monometallic catalysts. Additionally, slight shifts in the higher 2θ angles indicate lattice strain or distortion in the CuO structure, likely due to interactions with the clay. The incorporation of clay restricts the growth of CuO crystallites, acting as a physical barrier and resulting in smaller crystallite sizes, which leads to peak broadening and further shifts in the XRD pattern. Overall, the presence of clay influences both the position and width of the XRD peaks, with the smaller-angle peaks attributed to the clay structure and the broader peaks reflecting changes in the crystallite size and lattice structure of CuO [21].

The calculated crystallite sizes for CuO NPs (**1**) and clay-supported CuO NCPs (**2**) are 11.73 nm and 11.97 nm, respectively. This similarity in sizes suggests that the presence of the clay support does not notably influence the crystal size of CuO. The average crystallite sizes (D) of the particles were determined using the Debye-Scherrer equation:

$$D = \frac{k\lambda}{\beta \cos\theta} \tag{6}$$

In Eq. (6), D represents the average crystallite size, k is the shape factor (commonly taken as 0.9), λ is the wavelength of the X-ray (0.15406 nm for Cu target Kα radiation), β is the width at half-maximum (FWHM) of the diffraction peak, and θ is the Bragg diffraction angle. These findings suggest that both synthesized photocatalysts (**1**) and (**2**) possess well-defined crystalline structures, as indicated by the sharp diffraction peaks at the (111) plane and the calculated crystallite sizes. The consistency in the crystalline nature and size across both materials underscores the successful synthesis of CuO NPs (**1**) and their clay-supported CuO NCPs (**2**). Consequently, the most intense (111) peaks in the XRD patterns were used to calculate the average crystallite size (D) for both photocatalysts, as summarized in Tables 2 and 3 below.

Overall, to deconvolute the contributions of crystallite size and lattice strain to peak broadening, Williamson-Hall (W-H) analysis was performed using the uniform deformation model: $\beta\cos\theta = (k\lambda/D) + (4\varepsilon \sin\theta)$, where ε is the lattice strain. From the W-H plots ($\beta\cos\theta$ vs. $4\sin\theta$), the intercept yields $k\lambda/D$ and the slope yields ε. For CuO NPs (**1**), the W-H analysis gave a crystallite size of 10.8 ± 1.2 nm (consistent with the Debye-Scherrer average of 11.73 nm) and a lattice strain of 0.0032 ± 0.0005 (dimensionless). For clay-supported CuO NCPs (**2**), the crystallite size was 11.2 ± 1.0 nm (comparable to the Debye-Scherrer value of 11.97 nm) with a slightly higher lattice strain of 0.0041 ± 0.0006. The increased strain in the clay-supported sample likely arises from lattice distortion at the CuO-clay interface due to mismatched lattice parameters and differential thermal expansion during calcination at 450 °C. This interfacial strain may influence the electronic structure and, consequently, the photocatalytic behavior, though the precise effect

Table 2
Selected XRD analysis of numerical values and average crystal size (nm) of CuO NPs (**1**).

2θ (degree)	2θ/2 (degree)	FWHM	2θ/2 (radian)	β(radian)	Crystal size (nm)	Average size (nm)
16.61	8.306	0.263	0.145	0.00459	30.517	
22.89	11.445	0.292	0.199	0.00510	27.725	
35.61	17.806	0.711	0.311	0.0124	**11.732**	= 10.06
38.83	19.415	1.005	0.338	0.0175	8.381	
48.83	24.41	0.979	0.426	0.0170	8.911	
61.57	30.788	0.784	0.537	0.0136	11.787	
66.85	33.423	2.338	0.583	0.0408	4.070	**Total = 14.73**

Table 3
Selected XRD analysis of numerical values and average crystal size (nm) of clay-supported CuO NCPs (**2**).

2θ(degree)	2θ/2 (degree)	FWHM	2θ/2 (radian)	β(radian)	Crystal size (nm)	Average size (nm)
35.59	17.796	0.648	0.3106	0.0113	12.866	
38.86	19.429	0.703	0.339	0.0122	**11.975**	
48.65	24.328	0.917	0.424	0.0160	9.501	= 11.20
58.36	29.183	0.705	0.509	0.0123	12.898	
61.64	30.822	0.780	0.537	0.0136	11.847	
66.19	33.099	0.963	0.577	0.0168	9.847	
68.233	34.116	0.847	0.595	0.0147	11.328	**Total = 11.466**

Table 4
EDX result of CuO NPs (**1**).

Elements	Line type	Apparent Concentration	Wt%	Wt% Sigma	Atomic Percent	Standard Sample level
C	K	10.01	39.03	0.38	61.74	C
O	K	17.88	22.18	0.27	**26.34**	SiO_2
S	K	0.95	1.11	0.06	0.66	FeS_2
Cu	L	20.95	37.69	0.34	**11.27**	Cu
Total			**100**		**100**	

Table 5
EDX result of clay-supported CuO NCPs (**2**).

Elements	Line type	Apparent Concentration	Wt%	Wt% Sigma	Atomic Percent	Standard Sample level
C	K	11.11	41.92	0.34	65.05	C
O	K	15.35	20.27	0.23	23.61	SiO_2
Mg	K	0.04	0.08	0.05	0.06	MgO
Si	K	0.4	0.55	0.04	0.36	SiO_2
Ca	K	0.01	0.01	0.04	0.01	Wollastonite
Fe	K	0.24	0.32	0.1	0.11	Fe
Cu	L	20	36.85	0.29	10.81	Cu
Total			**100**		**100**	

requires further investigation through techniques such as Raman spectroscopy or high-resolution TEM. Based on the Debye-Scherrer analysis of the most intense (111) diffraction peaks, the average crystallite sizes were 11.73 nm for CuO NPs (1) and 11.97 nm for clay-supported CuO NCPs (2). Williamson-Hall analysis, which accounts for both size and strain broadening, yielded mean crystallite sizes of 10.8 ± 1.2 nm and 11.2 ± 1.0 nm, respectively, confirming that the two methods are in good agreement.

3.4. Surface morphology (SEM) analysis

The surface morphology of CuO NPs (**1**) and clay-supported CuO NCPs (**2**) was examined using a JCM-6000 Plus scanning electron microscope (SEM) at various magnifications (Fig. 5). The SEM images of CuO NPs (**1**) (Fig. 5a–e) reveal irregular, agglomerated secondary particles ranging from 100 nm to 5 μm. This agglomeration is typical for unsupported metal oxide nanoparticles synthesized by co-precipitation due to high surface energy. It is crucial to distinguish this agglomerate size from the primary crystallite size. The XRD analysis (Section 3.3, Tables 2 and 3) determined the average primary crystallite size to be ~11–12 nm for both samples. The much larger structures observed in SEM are secondary agglomerates composed of many primary crystallites. In contrast, the clay-supported CuO NCPs (**2**) (Fig. 5f–j and 7) show a more dispersed morphology, with smaller agglomerates (50 nm to 1 μm) distributed across the layered clay surface [46]. The clay matrix appears as flake-like structures typical of smectite clays, with CuO particles adhering to the clay surface and edges. This improved dispersion is attributed to the physical barrier provided by the clay layers, which prevents direct contact and agglomeration of CuO NPs [22,47]. The SEM-EDX elemental mapping (Tables 4 and 5, Figs. 6 and 7) confirms the presence of Cu, O, Si, Al, and Mg, with Cu signals colocalized with clay elements, suggesting reasonably uniform distribution at the micrometer scale. In addition, a clear distinction must be made between crystallite size, primary particle size, and agglomerate size when interpreting structural data. XRD analysis indicates similar crystallite sizes (~11–12 nm) for both CuO NPs and clay-supported CuO NCPs, representing the coherently diffracting domains (Fig. 4). However, SEM reveals significant differences in agglomeration behavior. Unsupported CuO NPs exhibit large agglomerates (~100 nm to 5 μm) due to high surface energy and the absence of stabilizing agents, which promotes particle clustering. In contrast, the clay-supported system shows reduced agglomeration (~50 nm to 1 μm) and more uniform particle distribution, as the clay matrix acts as a physical barrier that limits particle–particle interaction (Fig. 5). Despite this improvement, complete dispersion of individual crystallites is not achieved, which is typical for

co-precipitation methods without advanced dispersion control. These observations highlight the role of the clay support in improving morphological uniformity and potentially enhancing surface accessibility compared to unsupported CuO NPs [21,22].

3.5. EDX analysis

The purity and elemental composition of the nanomaterials were determined using energy-dispersive X-ray (EDX) spectroscopy. The EDX results, presented in Figs. 6 and 7, confirm the presence of copper and oxygen, validating the formation of CuO nanoparticles. The purity of the synthesized CuO NPs (**1**) is supported by the EDX spectrum shown in Table 4. Traces of sulfur are attributed to sulfate impurities, while carbon signals are likely due to the ethanol solvent used during synthesis. To achieve a purer sample, repeated washing with distilled water is recommended to remove residual sulfur and carbon. The weight percentages of copper and oxygen in photocatalyst (**1**) were found to be 37.69% and 22.18%, respectively. The corresponding atomic percentages of copper and oxygen were calculated to be 11.27% and 26.34%, respectively, indicating a uniform distribution of these elements in the CuO structure [44].

Fig. 7 presents the EDX analysis of clay-supported CuO NCPs (**2**), confirming the presence of C, O, Mg, Si, Ca, Fe, and Cu as the primary components, thus indicating the formation of the nanocomposite with the respective elements. The weight and atomic compositions of these elements are detailed in Table 5. In conclusion, the CuO NPs (**1**) appear to be the dominant phase in the clay-supported CuO NCPs (**2**), with clay particles present in relatively small quantities, potentially as a thin layer or unevenly distributed. This could result in a weaker EDX signal from the clay elements, as clay primarily serves as a support material rather than a major constituent. Furthermore, elements such as Si, Al, Mg, Ca, and Fe from the clay may be present in trace amounts, given that clay is typically used in limited quantities that do not significantly impact the overall elemental composition. Consequently, the low concentration of clay may produce a faint EDX signal, with CuO NPs more abundantly represented in the analyzed regions, leading to lower concentrations of clay elements in these areas.

Overall, EDX analysis (Tables 4 and 5) reveals a high apparent carbon content (39–42 wt%) in both samples, likely arising from residual carbon species retained within the clay structure and contributions from carbon coating/tape during measurement. The measured Cu content is similar for CuO NPs (37.69 wt%) and clay-supported CuO (36.85 wt%), despite the latter having a much lower theoretical CuO loading (~9 wt% based on the synthesis ratio). This discrepancy indicates that EDX results are not representative of the bulk composition, but rather reflect localized, Cu-rich regions due to the limited analysis volume (~1 μm) relative to sample heterogeneity. Additionally, attenuation of X-rays from lighter elements (e.g., Si, Al, Mg) by carbon-based mounting materials further biases the results toward higher apparent Cu content [12]. These findings highlight the limitations of EDX for quantitative bulk analysis in heterogeneous nanocomposites.

3.6. BET surface area analysis

The surface area of materials plays a critical role in their performance as adsorbents, catalysts, and catalyst supports. In this study, three related materials were characterized: raw natural clay (smectite-rich), pure CuO NPs, and clay-supported CuO NCPs. The Brunauer–Emmett–Teller (BET) model was employed to determine the surface area, pore size, and pore volume of the Ethiopian smectite clay, CuO NPs (**1**), and clay-supported CuO NCPs (**2**), which are tabulated in Table 6.

The surface area and porosity data presented in Table 6 reveal crucial insights into the structural evolution and photocatalytic implications of the synthesized materials. Raw smectite clay exhibits a moderate BET surface area of 73.67 m^2/g with a total pore volume of 0.156 cc/g and an average pore diameter of 8.47 nm, characteristic of mesoporous 2:1 layered aluminosilicates with interlayer and interparticle voids. Upon synthesis of unsupported CuO NPs (1), a significant reduction in surface area to 27.05 m^2/g was observed, accompanied by a decrease in pore volume to 0.094 cc/g and an increase in average pore diameter to 13.90 nm. This behavior is typical for aggregated metal oxide nanoparticles, where primary nanocrystallites (11–12 nm from XRD) assemble into larger secondary agglomerates, creating larger interparticle macropores while drastically reducing the accessible micro- and mesopore volume [46,48]. While the increased surface area (36.14 vs. 27.05 m^2/g) and pore volume (0.132 vs. 0.094 cc/g) of the clay-supported composite compared to unsupported CuO provide a structural basis for the observed enhancement in decolorization efficiency (Table 6), we caution that surface area alone does not guarantee improved photocatalytic activity. Other factors, including light absorption efficiency, charge carrier separation, surface defect density, and mass transport limitations, also play critical roles. Notably, the clay-supported CuO NCPs (2) recovered a substantially higher surface area of 36.14 m^2/g and pore volume of 0.132 cc/g compared to unsupported CuO, while maintaining a large average pore diameter of 14.61 nm. This represents a 33.6% increase in surface area relative to unsupported CuO, directly demonstrating that the smectite clay matrix acts as an effective physical spacer, preventing excessive CuO nanoparticle agglomeration and preserving a porous network. The fractal dimension values (clay: 2.61, CuO NPs: 2.72, CuO NCPs: 2.68) indicate that all three materials possess rough, irregular surfaces typical of mesoporous systems, with unsupported CuO showing the highest surface irregularity due to uncontrolled aggregation. These findings align closely with recent literature:

Table 6
Textural properties derived from N_2 adsorption-desorption isotherms for clay, CuO NPs, and clay-supported CuO NCPs.

Sample	BET Surface Area (m^2/g)	Total Pore Volume (cc/g)	Average pore Diameter (nm)	Fractal Dimension
Raw smectite clay	73.67	0.156	8.47	2.61
CuO NPs (**1**)	27.05	0.094	13.90	2.72
Clay-CuO NCPs (**2**)	36.14	0.132	14.61	2.68

Chagour et al. (2025) reported a similar enhancement from 24.8 m^2/g for unsupported CuO to 38.2 m^2/g for clay-supported CuO, attributing the improvement to the exfoliation effect of clay platelets [21,27]. Similarly, Fatimah et al. (2022) demonstrated that montmorillonite-supported CuO achieved surface areas of 40–85 m^2/g depending on loading, with optimal photocatalytic performance observed at intermediate surface areas where dye adsorption and light penetration are balanced [12]. The hierarchical porosity observed in CuO NCPs (2), combining the intrinsic micropores/mesopores of the clay host with larger interparticle voids from CuO nanoparticle assemblies, is particularly advantageous for photocatalysis. This structure facilitates rapid mass transport of MG dye molecules to active sites while providing multiple light scattering pathways, enhancing photon absorption efficiency. In comparison, commercially available synthetic supports like graphene oxide (typically >200 m^2/g but at >100× higher cost) or activated carbon (800–1500 m^2/g but with poor thermal stability during calcination) offer higher surface areas but lack the synergistic cation-exchange and structural stabilization properties of natural smectite clay [47,49]. The intermediate surface area of 36.14 m^2/g for CuO NCPs (2) represents an optimal balance: sufficient for good dye adsorption and CuO dispersion, yet not so high as to cause excessive light scattering or electron trap recombination. This structural advantage directly explains the superior photocatalytic decolorization efficiency of clay-supported CuO NCPs (89.67%) compared to unsupported CuO NPs (82.96%), as the improved surface area and pore architecture enhance adsorption capacity and provide more accessible active sites for photocatalytic reaction. We note, however, that surface area measurements alone do not directly demonstrate improved charge carrier separation; such claims would require complementary techniques such as PL or EIS spectroscopy, which were not performed in this study. These results confirm that locally sourced Ethiopian smectite clay serves as an effective, low-cost support for engineering high-performance CuO-based photocatalysts for wastewater remediation.

3.7. Photocatalytic decolorization of MG dye using as-synthesized photocatalysts

The UV-Vis spectral analysis of MG dye decolorization using CuO NPs (**1**) and clay-supported CuO NCPs (**2**) demonstrates the effectiveness of both catalysts in dye removal under tungsten lamp irradiation, as a function of contact time, as shown in Fig. 8(a) and 9 (a). The UV-Vis spectrum of the MG solution exhibits a prominent absorption peak at 617 nm, consistent with previous studies [50]. During the decolorization process, a new peak around 425 nm emerges, signifying the breakdown of MG dye molecules through photodecolorization. The absorbance of the dye decreases over time, with a rapid initial decolorization phase followed by a slower rate of decolorization. This decrease in rate occurs as the available surface-active sites on the catalysts become increasingly occupied by dye molecules [51]. Before irradiation, each reaction mixture was stirred in the dark for 30 min to establish adsorption-desorption equilibrium. In the preliminary experiment (optimization), the adsorption kinetics were monitored by taking samples every 5 min during this dark period. Adsorption of MG onto CuO NPs (1) reached equilibrium after approximately 20 min, with a maximum adsorption of 9.8 ± 0.9% of the initial dye concentration. For clay-supported CuO NCPs (2), adsorption reached equilibrium after 25 min with slightly higher adsorption (11.3 ± 1.2% removal). For comparison, pure clay under dark conditions adsorbed 8.5 ± 1.1% of MG. The decolorization percentages reported in Fig. 8b and 9b are calculated relative to the concentration at the start of irradiation, not the initial concentration before adsorption. This is why the decolorization at t = 0 appears as 0% in the figures. The separation between adsorption and photocatalysis is essential for accurately assessing the photocatalytic activity. After correcting for adsorption contributions (9.8% for CuO NPs and 11.3% for CuO NCPs) and photolysis (4.2% for MG alone under light without catalysts), the net

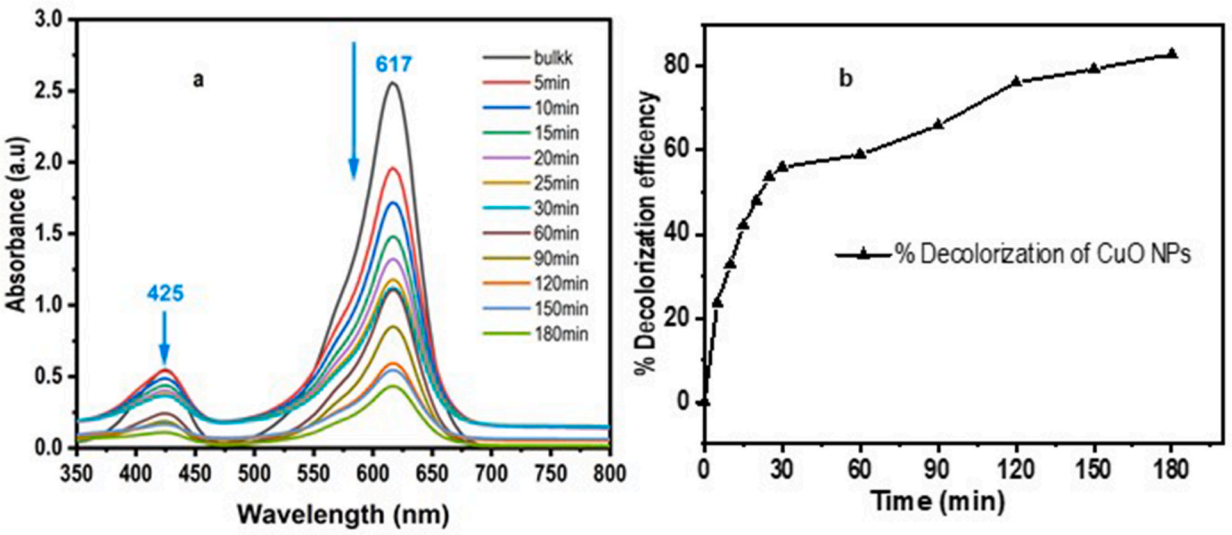

Fig. 8. (a) UV-Vis spectral changes of MG dye during photocatalytic decolorization using CuO NPs (**1**) under tungsten lamp (200 W) irradiation. During the first 30 min (dark equilibration), spectra were recorded every 5 min. After illumination started, spectra were recorded every 30 min up to 180 min. (b) Corresponding percentage decolorization as a function of time.

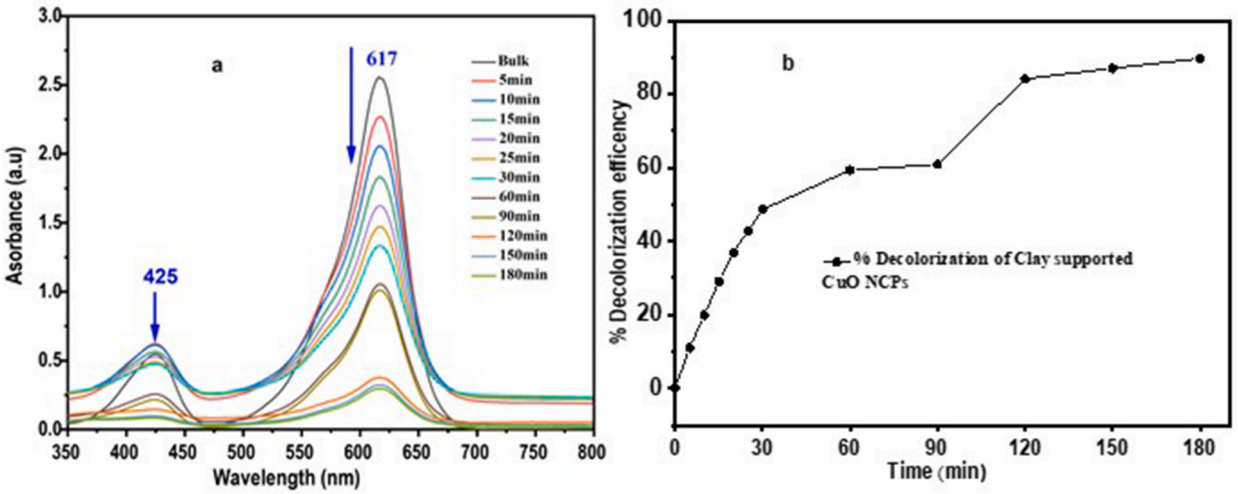

Fig. 9. (a) UV-Vis spectral changes of MG dye during photocatalytic decolorization using CuO NCPs (**2**) under tungsten lamp (200 W) irradiation. During the first 30 min (dark equilibration), spectra were recorded every 5 min. After illumination started, spectra were recorded every 30 min up to 180 min. (b) Corresponding percentage decolorization as a function of time.

photocatalytic removal is 68.9% for CuO NPs and 74.2% for clay-supported CuO over 180 min. This confirms that photochemical processes dominate the observed decolorization, though adsorption plays a non-negligible role, particularly for the clay-supported CuO NCPs, which have higher surface energy and greater tendency for dye binding.

A comparison of the MG dye decolorization efficiencies between CuO NPs (**1**) and clay-supported CuO NCPs (**2**) shows that, after 180 min of irradiation (Fig. 8(a), (b), and 9(a), (b)), CuO NPs achieve a decolorization efficiency of 82.96%, while the clay-supported CuO NCPs exhibit a slightly higher efficiency of 89.67%. Comparison with literature shows that our clay-supported CuO NCPs (**2**) achieves 89.67% decolorization, which is comparable or superior to many previously reported systems under similar conditions. For example, Chagour et al. [21] reported 94% decolorization of MG (10 ppm) using CuO/kaolin under a halogen lamp, while our system achieved 89.67% at a higher MG concentration (20 ppm). The rate constant for clay-CuO (0.0112 min^{-1}) is lower than the 0.025 min^{-1} reported by Chagour et al., possibly due to differences in light source (tungsten vs. halogen) and catalyst loading (0.328 vs. 1.0 g/L). Our clay-CuO outperforms unsupported CuO NPs by approximately 7% absolute (89.67% vs. 82.96%), consistent with the enhancement reported in most clay-supported systems. The enhanced performance of the clay-supported catalyst is attributed to improved nanoparticle dispersion and increased accessible surface area provided by the clay support, which likely enhances adsorption capacity and provides more active sites for photocatalytic reaction. We note that the term *synergistic effects* implies cooperative interactions beyond simple additive contributions; such effects were not experimentally demonstrated in this study and should not be claimed without additional evidence (e.g., comparison to physical mixtures of clay and CuO NPs at equivalent ratios). This finding is in line with previous research, which indicates that smaller nanoparticle sizes are correlated with higher photocatalytic efficiency in dye decolorization [52,53]. In general, it is important to note that decolorization (disappearance of color) does not necessarily equate to complete degradation or mineralization. The decrease in absorbance at 617 nm indicates destruction of the triphenylmethane chromophore, but intermediates may remain in solution. Without TOC or COD analysis, we cannot claim complete mineralization to CO_2 and H_2O. Therefore, we use the term *decolorization* throughout this manuscript to accurately reflect the scope of our measurements.

The photodecolorization efficiency of the catalyst for MG dye was calculated using the relationships defined in Eqs. (3) and (4). Since absorbance (A) is directly proportional to concentration, the percentage of decolorization can be determined from the UV-Vis spectrum. A decrease in absorbance at the maximum wavelength (λ_{max}, 617 nm for MG) over time reflects the decolorization efficiency of photocatalysts (**1**) and (**2**). The rate of dye decolorization at a given time (t) was calculated using Eq. (4), and the reaction followed pseudo-first-order kinetics. The rate constant (k) was derived from a plot of ln(Ct/Co) versus time. The decolorization process involves the generation of hydroxyl radicals (•OH) and superoxide radicals (O^{2-}), which are crucial in the oxidation of MG dye molecules. When photons with energy equal to or greater than the bandgap of the clay-supported CuO NCPs (**2**) are absorbed, they excite electrons from the valence band (VB) to the conduction band (CB), generating electron-hole pairs. The photogenerated holes in the valence band then form hydroxyl radicals, while the conduction band electrons interact with oxygen to produce superoxide radicals. Both hydroxyl and superoxide radicals are highly reactive oxidants that attack and degrade MG dye molecules, leading to their mineralization and decolorization. Additionally, these radicals contribute to the elimination of microorganisms present in the medium. As described in Eqs. (7)–(13), the generation of electron-hole (e^-/h^+) pairs illustrates the photocatalytic reactions, with carbon dioxide and water being the end products of the decolorization process, as observed in various studies [9,54]. In general, the decolorization of malachite green dye using CuO nanocomposites begins with the adsorption of the dye molecules onto the surface of the CuO nanoparticles. Once adsorbed, the CuO nanocomposites, when exposed to light or in the presence of oxygen and water, generate reactive oxygen species (ROS), including hydroxyl radicals (•OH), superoxide anions (O_2•$^-$), and singlet oxygen ($^1O_2$). These

highly reactive species attack the chromophore of the MG dye (triphenylmethane structure, which includes two *N, N*-dimethylaminophenyl groups and a central carbon atom), breaking the molecular structure and initiating oxidative decolorization. As a result, the dye molecules are fragmented into smaller, less toxic products through various radical reactions. Over time, these intermediates undergo further breakdown, leading to the complete mineralization of the dye into harmless by-products, such as carbon dioxide (CO_2) and water (H_2O), effectively removing the dye and reducing the toxicity of the treated water. This process involves a combination of oxidation and reduction mechanisms, driven by the interaction between CuO nanocomposites and the dye molecules. The following reaction mechanism (Eqs. (7)–(13)) is proposed *hypothetically* based on analogous CuO-based photocatalysis systems reported in the literature [55,56]. We emphasize that this mechanism is speculative and is presented only as a plausible pathway consistent with established photocatalysis principles. The identification of specific reactive species (•OH, O_2•$^-$, $^1O_2$, HO_2•) and the confirmation of the degradation pathway would require experimental validation using scavenger tests (e.g., using tert-butyl alcohol for •OH, p-benzoquinone for O_2•$^-$, and sodium azide for $^1O_2$), electron spin resonance (ESR/EPR) spectroscopy, and LC-MS or GC-MS analysis for intermediate identification. None of these experiments was performed in this study. Therefore, the mechanism described below should be considered as a literature-informed hypothesis, not as experimentally demonstrated conclusions for our specific system. Therefore, without scavenger experiments, we cannot definitively assign the participation of specific reactive oxygen species. Similarly, claims regarding reduced electron-hole recombination or enhanced charge separation are speculative in the absence of photoluminescence (PL) spectroscopy or electrochemical impedance spectroscopy (EIS) measurements.

$$MG_{(aq)} \xrightarrow[2.\ Clay-\text{sup}\ ported\ CuO\ NCPs]{1.\ CuO\ NPs} MG_{(adsorbed)} \tag{7}$$

$$CuO\ NPs/Clay-\text{sup}\ ported\ CuO\ NCPs + H_2O \rightarrow CuO\ NCPs \cdot H_2O \rightarrow CuO\ NCPs \cdot H_2O + \cdot OH \tag{8}$$

$$O_2 + e^- \rightarrow O_2^{\cdot -} \tag{9}$$

$$O_2 + h\nu \rightarrow {}^1O_2 \tag{10}$$

$$MG_{(adsorbed)} + \cdot OH \rightarrow Decolorized\ \text{intermediates}\ (\text{e.g., } quinones, aniline, carboxylic\ acids, etc.) \tag{11}$$

$$MG_{(adsorbed)} + O_2^{\cdot -} \rightarrow Decolorized\ \text{intermediates} \tag{12}$$

$$Decolorized\ intermediates + \cdot OH \rightarrow CO_2 + H_2O + Nontoxic\ fragments\ (e.g., benzoic\ acid, formic\ acid, etc.) \tag{13}$$

According to literature reports for analogous CuO-based photocatalysis systems, superoxide radicals may aid the oxidation process. However, we did not perform any experiments to assess electron-hole recombination rates (e.g., PL, transient photocurrent response, or EIS). Therefore, statements regarding recombination suppression are speculative and should not be inferred from the decolorization data alone. Superoxide is protonated in this step, leading to the production of H_2O_2. During the prior step, superoxide ions were formed. These further dissociate and produce a hydroxyl radical, which is very volatile. The oxidation and reduction reactions occur concurrently on the photoexcited surface of photocatalysts (**1**) and (**2**). Which means, in AOPs for the decolorization of MG dye using clay-supported CuO NCPs (**2**) and CuO NPs (**1**), several reactive radicals are involved in the decolorization process. The main radicals, such as ·OH, superoxide (O_2·$^-$), singlet oxygen ($^1O_2$), and perhydroxyl (HO_2·), all play vital roles in breaking down the dye molecules. The interaction between CuO NPs and hydrogen peroxide or oxygen leads to the generation of reactive radicals, which subsequently attack the dye molecules, resulting in oxidative decolorization. Copper species (Cu^+/Cu^{2+}) also play a crucial role in the catalytic cycle, further enhancing the decolorization process. The combined action of these radicals significantly increases the overall dye decolorization efficiency, positioning clay-supported CuO NPs as a promising material for environmental remediation and wastewater treatment applications [21,23]. The study suggests that smaller nanoparticle sizes improve photocatalytic decolorization efficiency, as they provide larger surface areas and more active sites for interaction with dye molecules. Clay-supported CuO NCPs (**2**) may show improved dispersion and reduced agglomeration compared to standalone CuO NPs (**1**), though reusability studies and post-reaction characterization were not performed to confirm stability. A detailed analysis of the UV-Vis spectra confirms the effectiveness of both photocatalysts for the decolorization of MG dye. The modest enhancement observed for clay-supported CuO NCPs (**2**) relative to unsupported CuO NPs (**1**) is consistent with improved nanoparticle dispersion and increased surface area provided by the clay matrix. Claims regarding modified electronic properties or synergistic catalytic effects would require additional evidence (e.g., XPS for electronic structure) and are not supported by the current data. Furthermore, the porous nature of clay provides a large surface area, ensuring uniform dispersion of CuO NPs and increasing the number of active sites available for catalytic reactions, thereby accelerating the reaction rates. The clay also serves to stabilize the nanoparticles, preventing agglomeration or sintering, which helps preserve their surface area and catalytic activity over time. Additionally, the clay support offers a protective environment that extends the lifespan of the nanoparticles, ensuring long-term catalyst effectiveness and durability [25,37]. Overall, reusability studies and post-reaction catalyst characterization were not performed in this study. Typically, reusability is assessed through multiple decolorization cycles (e.g., 5-10 cycles) with the same catalyst, with characterization (XRD, BET, FTIR, SEM) before and after use to assess structural stability, and measurement of copper leaching to ensure heterogeneous catalysis [12,21]. Without these data, claims of improved stability

are premature. In addition, a critical control for heterogeneous photocatalysis is the evaluation of metal leaching. If Cu^{2+} ions leach into solution, they could act as homogeneous photocatalysts or Fenton-like reagents, contributing to dye decolorization independently of the solid catalyst. We did not perform ICP-OES or AAS analysis to quantify copper leaching in this study. Therefore, we cannot definitively conclude that the observed decolorization is purely heterogeneous.

Comparison with literature (Table 7) shows that our clay-supported CuO NCPs (89.7% decolorization, 0.0112 min^{-1}) perform comparably to other clay-supported systems [21], though less efficiently than more complex heterojunctions [14,15]. The lower rate constant compared to Chagour et al. [21] (0.0250 min^{-1}) likely reflects differences in light source intensity (halogen vs. tungsten), catalyst loading (1.0 vs. 0.328 g/L), and initial dye concentration (10 vs. 20 ppm). Direct quantitative comparisons should be made cautiously due to variations in experimental conditions.

3.8. Kinetic studies of photocatalytic decolorization of MG dye

As shown in Fig. 10(a) and (b), the linear relationship observed in the plots of $\ln(C_0/C_t)$ versus time confirms that the photodecolorization of MG follows pseudo-first-order kinetics for both CuO NPs (**1**) and clay-supported CuO NCPs (**2**) under irradiation from a 200 W tungsten lamp. All kinetic measurements were conducted in triplicate, and the associated errors were calculated as standard deviations. The determined rate constants were $k = 0.0094 \pm 0.0012\ min^{-1}$ ($t_1/_2 = 73.7 \pm 9.4$ min, $R^2 = 0.9143$) for CuO NPs and $k = 0.0112 \pm 0.0010\ min^{-1}$ ($t_1/_2 = 61.9 \pm 5.5$ min, $R^2 = 0.9625$) for the clay-supported CuO NCPs, with the difference in rate constants being statistically significant ($p = 0.012$, paired *t*-test, $n = 3$). The relatively high correlation coefficients indicate good agreement with the pseudo-first-order kinetic model, noting that R^2 reflects the quality of model fitting rather than adsorption behavior. The higher R^2 value for the clay-supported system (0.9625 vs. 0.9143) suggests a more consistent kinetic profile, which may be attributed to improved dispersion and reduced agglomeration of CuO nanoparticles on the clay support (as observed by SEM, Fig. 5). Alternative explanations, such as reduced electron-hole recombination or enhanced charge transfer, cannot be evaluated from kinetic data alone and would require direct measurement techniques (e.g., PL, EIS). For comparison, the data were also analyzed using the pseudo-second-order model ($t/q_t = 1/k_2q_e^2 + t/q_e$), which resulted in poorer fits (R^2 = 0.85–0.91), consistent with expectations for dilute dye systems (20 ppm) where first-order kinetics generally predominate.

The energy consumption for photocatalytic processes using CuO nanoparticles (**1**) and clay-supported CuO (2) was 0.6 kWh, with an energy consumption rate of 6 kWh per kilogram of dye treated. For treating 0.1 kg of MG dye, the energy cost was $0.066, and the cost per kilogram of dye treated was $0.66. However, the energy and cost calculation was presented as a theoretical extrapolation to demonstrate the potential feasibility of scaling up the process, not as an experimentally determined value. Comparisons with literature studies were well aligned, providing a clear assessment of the efficiency and cost-effectiveness of CuO nanocomposites in dye decolorization [56]. To summarize, selecting the appropriate light source wavelength and intensity is crucial for achieving successful photocatalysis. When designing experiments, the light source's characteristics and exposure conditions should be considered to enhance efficiency and selectivity. In this study, tungsten fluorescent lamps are used due to their broad light spectrum and cost-effectiveness. However, for high-intensity UV activation, mercury vapor lamps or LEDs are better options, while xenon arc lamps, though powerful, are typically reserved for specialized, high-cost applications (Table 8) [56,57].

Recent studies have shown that CuO and clay-supported CuO NCPs have been synthesized for various applications using different methods. Chuaicham et al. [47]. reported that clay-based photocatalyst composites have gained significant attention in photocatalysis due to their abundance, excellent light absorption, and stability. Asamoah et al. [22]. developed cost-effective clay-metal oxide/metal (CuO/Ag and ZnO/Ag) composite pellets for efficient water purification. In this case, clay with inherent antibacterial properties acted as a support membrane for metal oxide/Ag nanoparticle concentrations (2.5, 5, and 10 wt%) as the active fillers. While clay/CuO/Ag pellets outperformed clay/ZnO/Ag pellets under various test conditions, their performance varied in nutrient-rich environments compared to those lacking bacterial growth nutrients. The highest diffraction peaks were observed at the 2θ values reported by Mobarek et al. [46]. Velsankar et al. [48]. and Philip et al. [58]. correspond to the (111) crystal plane, as per JCPDS card number 00-041-0254. These XRD results were consistent with our synthesized CuO NPs (**1**) and clay-supported CuO NCPs (**2**), with diffraction peaks at 35.61° and 38.86°, respectively. Both (**1**) and (**2**) exhibited a polycrystalline structure and were identified as monoclinic tenorite phase CuO. The average crystal sizes were 11.73 nm for (1) and 11.97 nm for (2), which are slightly smaller than those previously reported. The pH of the reaction mixture is crucial as it influences both particle size and stability of the synthesized nanocomposite. Additionally, differences in synthesis methods and temperature can lead to variations in particle sizes, with smaller

Table 7
Comparison of MG dye decolorization using CuO-based photocatalysts reported in the literature.

Photocatalyst	MG Conc (ppm)	Catalyst loading (g/L)	Light source	Time (min)	Efficiency (%)	Rate constant (min^{-1})	Ref.
CuO NPs	10	1.0	Halogen lamp	180	78.0	0.0085	[21]
CuO NPs	10	0.4	UV lamp	120	76	0.008	[38]
CuO/kaolin	10	1.0	Halogen lamp	180	94.0	0.0250	[21]
$LaCeO_3$/CuO	10	0.5	Solar simulator	120	92.6	0.0198	[15]
CuO/BCN/MXene	20	0.4	Visible LED	90	98.3	0.0421	[14]
CuO/ montmorillonite	25	0.5	UV lamp	180	85	0.010	[12]
CuO NPs (**1**)	20	0.328	Tungsten lamp	180	82.9	0.0094	**This work**
Clay-CuO NCPs (**2**)	20	0.328	Tungsten lamp	180	89.7	0.0112	**This work**

Table 8
Different light sources are used for photocatalytic activities.

Feature	Tungsten fluorescent lamps (this work)	Mercury vapor lamps	LEDs (UV LEDs)	Xenon arc lamps
Light Spectrum	Broad (Visible)	Primarily UV (UV-A and UV-C)	Specific wavelengths (UV-C)	Very broad (UV, visible, IR)
Energy Efficiency	Moderate	High (but energy-consuming)	Very high	Low (Lots of heat)
Cost	Low	High	High	Very high
Best for	Moderate-intensity applications	High-intensity UV applications	Targeted UV photocatalysis	High-intensity, broad-spectrum applications

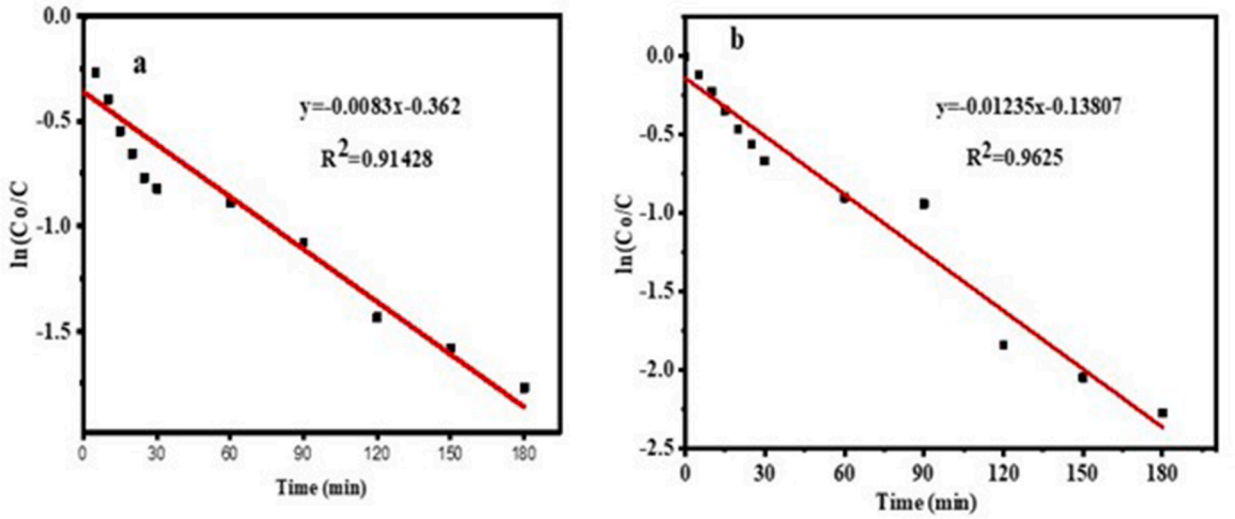

Fig. 10. Pseudo-first-order kinetic plot (ln(Ct/C0) vs. time) for the photocatalytic decolorization of MG dye using CuO NPs (**1**) (a) and clay-supported CuO NCPs (**2**) (b), respectively. Irradiation was provided by a 200 W tungsten fluorescent lamp.

particles showing a significantly higher surface-to-volume ratio [59].

In general, the structural characterization of clay-supported CuO NCPs (**2**) typically employs techniques such as XRD, SEM, and EDX, which provide detailed information about the phase composition, surface morphology, and elemental distribution of the material. These analyses confirm that CuO nanoparticles are uniformly distributed on or within the clay matrix. The interaction between the clay and CuO NPs is likely of a physical nature, with possible forces including van der Waals interactions or hydrogen bonding, rather than strong chemical bonds [60]. In some instances, surface interactions such as electrostatic forces or coordination bonds between CuO and the clay's silicate groups may further enhance nanoparticle stability, dispersion on the clay surface, and the overall performance of the composite material. Additionally, the surface functional groups of the clay may interact with dye molecules, further facilitating the sorption process. This interaction between the clay and CuO ensures effective coupling, thereby improving the material's properties for the decolorization of MG [38,45].

4. Conclusion

In conclusion, CuO NPs (**1**) and clay-supported CuO NCPs (**2**) were successfully synthesized via a simple co-precipitation method using $CuSO_4{\cdot}5H_2O$ as the precursor and locally sourced Ethiopian smectite clay as the supporting material. Comprehensive characterization using FTIR, UV-Vis, SEM-EDX, and XRD confirmed the formation of monoclinic CuO with average crystallite sizes of 11.73 nm and 11.97 nm, respectively. The optical band gap energies were calculated as 2.16 eV for CuO NPs (1) and 2.07 eV for clay-supported CuO NCPs (**2**) using the approximate method $Eg = 1240/\lambda$. Photocatalytic decolorization studies under a 200 W tungsten lamp (visible light) showed that clay-supported CuO NCPs (**2**) achieved 89.67 ± 1.4% decolorization of malachite green (20 ppm, pH 7) after 180 min, compared to 82.96 ± 1.8% for unsupported CuO NPs (**1**) under identical conditions. Adsorption during the 30-min dark equilibration period accounted for 9.8% and 11.3% of total removal, respectively, confirming that photochemical processes dominate the observed decolorization. The enhanced performance of the clay-supported composite is consistent with the observed improvements in nanoparticle dispersion (SEM, Fig. 5) and increased BET surface area (36.14 vs. 27.05 m^2/g, Table 6). While literature reports suggest that clay supports may also influence charge carrier dynamics, such effects were not directly measured in this study and should not be inferred from decolorization data alone. The decolorization kinetics followed pseudo-first-order behavior (R^2

= 0.9625 for clay-supported CuO). The enhanced performance of the clay-supported composite is consistent with literature reports suggesting that clay supports improve nanoparticle dispersion, increase available surface area, and potentially reduce electron-hole recombination. However, we note that BET surface area measurements, photoluminescence spectroscopy, and electrochemical impedance spectroscopy were not performed in this study to directly verify these mechanisms. Additionally, the decolorization of MG was monitored by UV-Vis absorbance at 617 nm; complete mineralization to CO_2 and H_2O was not confirmed by TOC or COD analysis. Scavenger experiments to identify reactive species and PL/EIS measurements to elucidate the catalytic mechanism were beyond the scope of this study and remain as critical directions for future work. Reusability studies, copper leaching evaluation, and scavenger tests for reactive species validation were beyond the scope of this work. Despite these limitations, this study demonstrates that locally sourced Ethiopian smectite clay is an effective and low-cost support for CuO nanoparticles, exhibiting enhanced photocatalytic decolorization activity compared to unsupported CuO. The co-precipitation method described is relatively simple and scalable, though it does utilize ethanol in the initial CuO NPs synthesis step. Future work should focus on: (i) systematic parametric optimization of operational conditions (pH, catalyst loading, initial dye concentration, light intensity), (ii) TOC/COD analysis to quantify mineralization, (iii) LC-MS identification of degradation intermediates, (iv) reusability studies over multiple cycles, (v) scavenger experiments to identify reactive species, and (vi) PL and EIS measurements to directly assess charge carrier separation and recombination dynamics an aspect that remains speculative in the current study. This approach presents a promising pathway for developing affordable and effective photocatalysts for wastewater treatment in resource-limited settings.

CRediT authorship contribution statement

Getu Worku Wudu: Writing – original draft, Visualization, Formal analysis, Data curation. **Belete Asefa Aragaw:** Writing – review & editing, Investigation, Data curation. **Alebel Nibret Belay:** Writing – review & editing, Validation, Supervision, Methodology, Investigation, Formal analysis, Conceptualization.

Data availability statement

Data included in the article/supplementary material are referenced in the article.

Declaration of competing interest

The authors declare that they have no known competing financial interests or personal relationships that could have appeared to influence the work reported in this paper.

Acknowledgments

The authors would like to express their sincere gratitude to the techniques that contributed to this research, especially to the work supported and grant-funded by the Minister of Education and Bahir Dar University (BDU), Ethiopia.

References

[1] A. Gezahegn, L.B. Merga, S. Mammo, Industrial effluents caused environmental pollution and its potential ecological and human health impacts in Ethiopia: a review, Waste Manag. Bull. 3 (4) (2025) 100240, https://doi.org/10.1016/j.wmb.2025.100240.
[2] N. Chausali, J. Saxena, R. Prasad, Nanotechnology as a sustainable approach for combating the environmental effects of climate change, J. Agric. Food Res. 12 (2023) 1000541, https://doi.org/10.1016/j.jafr.2023.100541.
[3] M. Saeed, M. Muneer, A.U. Haq, N. Akram, Photocatalysis: an effective tool for photodegradation of dyes-a review, Environ. Sci. Pollut. Res. 29 (1) (2022) 293–311, https://doi.org/10.1007/s11356-021-16389-7.
[4] G. Sarojini, S.V. Babu, N. Rajamohan, M. Rajasimman, Performance evaluation of polymer-marine biomass-based bionanocomposite for the adsorptive removal of malachite green from synthetic wastewater, Environ. Res. 204 (2022) 112132, https://doi.org/10.1016/j.envres.2021.112132.
[5] S. Velusamy, A. Roy, S. Sundaram, T.K. Mallick, A review on heavy metal ions and containing dyes removal through graphene oxide-based adsorption strategies for textile wastewater treatment, Chem. Rec. 21 (7) (2021) 1570–1610, https://doi.org/10.1002/tcr.202000153.
[6] S. Vigneshwaran, P. Sirajudheen, P. Karthikeyan, S. Meenakshi, Fabrication of sulfur-doped biochar derived from tapioca peel waste with superior adsorption performance for the removal of malachite green and Rhodamine B dyes, Surf. Interfaces 23 (2021) 100920, https://doi.org/10.1016/j.surfin.2020.100920.
[7] M. Anjum, R. Miandad, M. Waqas, F. Gehany, M.A. Barakat, Remediation of wastewater using various nano-materials, Arab. J. Chem. 12 (8) (2019) 4897–4919, https://doi.org/10.1016/j.arabjc.2016.10.004.
[8] G. Rajesh, P.S. Kumar, G. Rangasamy, S. Akilandeswari, A. Mandal, V.U. Shankar, M. Ramya, K. Nirmala, K. Thirumalai, Fabrication of a novel Ni-doped $CdAl_2O_4$ nanoparticles and applications in photo-oxidation processes under visible light illumination, Mol. Catal. 535 (2023) 112835, https://doi.org/10.1016/j.mcat.2022.112835.
[9] A. Ajmal, I. Majeed, R.N. Malik, H. Idrissi, M.A. Nadeem, Principles and mechanisms of photocatalytic dye degradation on TiO_2-based photocatalysts: a comparative overview, RSC Adv. 4 (70) (2014) 37003–37026, https://doi.org/10.1039/C4RA06658H.
[10] T. Welderfael, O.P. Yadav, A.M. Taddesse, J. Kaushal, Synthesis, characterization, and photocatalytic activities of Ag-N-codoped ZnO nanoparticles for degradation of methyl red, Bull. Chem. Soc. Ethiop. 27 (2) (2016) 221–232, https://doi.org/10.4314/bcse.v27i2.7.
[11] M.A. Khan, N. Nayan, Shadiullah, M.K. Ahmad, C.F. Soon, Surface study of CuO nanopetals by advanced nanocharacterization techniques with enhanced optical and catalytic properties, Nanomaterials 10 (2020) 1–18, https://doi.org/10.3390/nano10071298.
[12] S.I. Fatimah, G. Fadillah, I. Yanti, R.A. Doong, Clay-supported metal oxide nanoparticles in catalytic advanced oxidation processes: a review, Nanomaterials 12 (2022) 825, https://doi.org/10.3390/nano12050825.
[13] K. Aggarwal, A. Brahma, Nisha, Y. Sharma, P. Rajput, B. Sachdeva, A. Singh, R. Chandra, S. Singh, Recent progress in copper nanomaterials: catalysis, energy, biomedicine, and environmental applications, Mater. Adv. 6 (2025) 9296–9339, https://doi.org/10.1039/D5MA00484E.

[14] S. Mutahir, M.A. Khan, W.H. Liu, R. Butt, M. Humayun, L.Z. Meng, I. Shaheen, Engineering a dual Z-Scheme copper Oxide/Boron carbon Nitride/MXene heterojunction with tailored band alignment for high-efficiency photocatalytic degradation of refractory organic pollutants, J. Colloid Interface Sci. 691 (2025) 137442, https://doi.org/10.1016/j.jcis.2025.137442.
[15] R.D.F. Irbati, D.O.B. Apriandanu, M. Rahayu, V.R. Ananda, M.R. Yusuf, S. Chandren, Y. Yulizar, Green fabrication of novel $LaCeO_3$ decorated with CuO using Kigelia africana (lamb) benth leaf extract for photocatalytic degradation of malachite green, Nano-struct, Nano-Objects 42 (2025) 101474, https://doi.org/10.1016/j.nanoso.2025.101474.
[16] M.H.A. Hussain, G.S.P. Soylu, Metal oxide nanoparticles synthesized in ionic liquids: characterization and photodegradation of methyl Orange, ACS Omega 10 (2025) 9962–9975, https://doi.org/10.1021/acsomega.4c07627.
[17] M. Pirhashemi, A. Habibi-Yangjeh, Ultrasonic-assisted preparation of plasmonic ZnO/Ag/Ag_2WO_4 nanocomposites with high visible-light photocatalytic performance for degradation of organic pollutants, J. Colloid Interface Sci. 491 (2017) 216–229, https://doi.org/10.1016/j.jcis.2016.12.044.
[18] J. Chang, J. Ma, Q. Ma, D. Zhang, N. Qiao, M. Hu, H. Ma, Adsorption of methylene blue onto Fe3O4/activated montmorillonite nanocomposite, Appl. Clay Sci. 119 (2016) 132–140, https://doi.org/10.1016/j.clay.2015.06.038.
[19] C. Li, Z. Sun, W. Zhang, C. Yu, S. Zheng, Highly efficient g-C3N4/TiO2/kaolinite composite with novel three-dimensional structure and enhanced visible light responding ability towards ciprofloxacin and S. aureus, Appl. Catal. B Environ. 220 (2018) 272–282, https://doi.org/10.1016/j.apcatb.2017.08.044.
[20] J.A. Cecilia, C. García-Sancho, E. Vilarrasa-García, J. Jiménez-Jiménez, E. Rodriguez-Castellón, Synthesis, characterization, uses and applications of porous clays heterostructures: a review, Chem. Rec. 18 (7–8) (2018) 1085–1104, https://doi.org/10.1002/tcr.201700107.
[21] N. Chagour, E. Zouaoui, M. Boulkroune, D. Bouras, A.N.E. Houda Sid, S. Grigorian, G.A. El-Hiti, M. Fellah, Photocatalytic removal of malachite green using monometallic catalysts supported on clay, J. Water Process Eng. 72 (2025) 107573, https://doi.org/10.1016/j.jwpe.2025.107573.
[22] R.B. Asamoah, A. Yaya, P. Nbelayim, E. Annan, B.O. Agyeman, Development and characterization of clay-nanocomposites for water purification, Materials 13 (17) (2020) 3793, https://doi.org/10.3390/ma13173793.
[23] E.C. Okpara, O.B. Wojuola, T.W. Quadri, C.E. Banks, An overview of advanced oxidation processes using copper-based catalytic degradation of organic pollutants in water, Appl. Mater. Today 36 (2024) 102053, https://doi.org/10.1016/j.apmt.2023.102053.
[24] A. Bhatnagar, M. Sillanpää, Utilization of agro-industrial and municipal waste materials as potential adsorbents for water treatment-A review, Chem. Eng. J. 157 (2–3) (2010) 277–296, https://doi.org/10.1016/j.cej.2010.01.007.
[25] M. Rafatullah, O. Sulaiman, R. Hashim, A. Ahmad, Adsorption of methylene blue on low-cost adsorbents: a review, J. Hazard Mater. 177 (1–3) (2010) 70–80, https://doi.org/10.1016/j.jhazmat.2009.12.047.
[26] S.N. Tan, M.L. Yuen, R.A. Ramli, Photocatalysis of dyes: operational parameters, mechanisms, and degradation pathway, Green Anal. Chem. 12 (2025) 100230, https://doi.org/10.1016/j.greeac.2025.100230.
[27] K. Sharma, V. Dutta, S. Sharma, P. Raizada, A. Hosseini-Bandegharaei, P. Thakur, P. Singh, Recent advances in enhanced photocatalytic activity of bismuth oxyhalides for efficient photocatalysis of organic pollutants in water: a review, J. Ind. Eng. Chem. 78 (2019) 1–20, https://doi.org/10.1016/j.jiec.2019.06.022.
[28] M. Kashif, M. Yuan, Y. Su, P.M. Heynderickx, A. Memon, A review on pillared clay-based catalysts for low-temperature selective catalytic reduction of NOx with hydrocarbons, Appl. Clay Sci. 233 (2023) 106847, https://doi.org/10.1016/j.clay.2023.106847.
[29] M.H. Zhang, H. Dong, L. Zhao, D. Wang, D. Meng, A review on Fenton process for organic wastewater treatment based on optimization perspective, Sci. Total Environ. 670 (2019) 110–121, https://doi.org/10.1016/j.scitotenv.2019.03.180.
[30] A.N. Belay, M.E. Mihretu, T.G. Getnet, Synthesis, characterization, and antibacterial activities of Cu-Ag bimetallic oxide nanocomposites using Eichhornia crassipes aqueous leaf extract, J. Exp. Nanosci. 18 (1) (2023) 1–19, https://doi.org/10.1080/17458080.2023.2202911.
[31] A. Singh, N.B. Singh, I. Hussain, H. Singh, V. Yadav, Synthesis and characterization of copper oxide nanoparticles and its impact on germination of Vigna radiata (L.) R. Wilczek, Trop. Plant Res. 4 (2) (2017) 246–253, https://doi.org/10.22271/tpr.2017.v4.i2.034.
[32] F. Loosli, Z. Yi, J. Wang, M. Baalousha, Improved extraction efficiency of natural nanomaterials in soils to facilitate their characterization using a multimethod approach, Sci. Total Environ. 677 (2019) 34–46, https://doi.org/10.1016/j.scitotenv.2019.04.301.
[33] T.T. Zhu, C.H. Zhou, F.B. Kabwe, Q.Q. Wu, C.S. Li, J.R. Zhang, Exfoliation of montmorillonite and related properties of clay/polymer nanocomposites, Appl. Clay Sci. 169 (2019) 48–66, https://doi.org/10.1016/j.clay.2018.12.006.
[34] A.N. Belay, O.P. Yadav, I. Diaz, A.M. Taddesse, Cr-N co-doped ZnO nanoparticles: synthesis, characterization, and photocatalytic activity for degradation of thymol blue, Bull. Chem. Soc. Ethiop. 29 (2) (2015) 247–258, https://doi.org/10.4314/bcse.v29i2.8.
[35] C. Xu, L. Cao, G. Su, W. Liu, X. Qu, Y. Yu, Preparation, characterization and photocatalytic activity of Co-doped ZnO powders, J. Alloys Compd. 497 (2010) 373–376, https://doi.org/10.1016/j.jallcom.2010.03.076.
[36] R.Y. Hong, J.H. Li, L.L. Chen, D.Q. Liu, H.Z. Li, Y. Zheng, J. Ding, Synthesis, surface modification and photocatalytic property of ZnO nanoparticles, Powder Technol. 189 (2009) 426–432, https://doi.org/10.1016/j.powtec.2008.07.004.
[37] S.M. Padre, S. Kiruthika, S. Mundinamani, R.S. Surabhi, J.-R. Jeong, K.M. Eshwarappa, M.S. Murari, V. Shetty, M. Ballal, S.C. Gurumurthy, Mono- and bimetallic nanoparticles for catalytic degradation of hazardous organic dyes and antibacterial applications, ACS Omega 7 (39) (2022) 35023–35034, https://doi.org/10.1021/acsomega.2c03784.
[38] M.I. Said, A.A. Othmanb, E.M. Abd elhakeemb, Structural, optical and photocatalytic properties of mesoporous CuO nanoparticles with tunable size and different morphologies, RSC Adv. 11 (2021) 37801–37813, https://doi.org/10.1039/D1RA04780A.
[39] P. Kumar, G.K. Inwati, M.C. Mathpal, S. Ghosh, W.D. Roos, H.C. Swart, Defects induced enhancement of antifungal activities of Zn-doped CuO nanostructures, Appl. Surf. Sci. 560 (2021) 150026, https://doi.org/10.1016/j.apsusc.2021.150026.
[40] L.V. Bora, R.K. Mewada, Visible/solar light active photocatalysts for organic effluent treatment: fundamentals, mechanisms and parametric review, Renew. Sustain. Energy Rev. 76 (2017) 1393–1421, https://doi.org/10.1016/j.rser.2017.01.130.
[41] A. Bouafia, S.E. Laouini, Green synthesis of iron oxide nanoparticles by aqueous leaves extract of Mentha Pulegium L.: effect of ferric chloride concentration on the type of product, Mater. Lett. 265 (2020) 127364, https://doi.org/10.1016/j.matlet.2020.127364.
[42] S. Chabri, A. Dhara, B. Show, D. Adak, A. Sinha, N. Mukherjee, Mesoporous CuO–ZnO p–n heterojunction-based nanocomposites with high specific surface area for enhanced photocatalysis and electrochemical sensing, Catal. Sci. Technol. 6 (9) (2016), https://doi.org/10.1039/C5CY01573A, 3238-32.
[43] Y. Yang, X. Wang, F. Yang, B. Mu, A. Wang, Progress and future prospects of hemostatic materials based on nanostructured clay minerals, Biomater. Sci. 11 (23) (2023) 7469–7488, https://doi.org/10.1039/D3BM01326J.
[44] K. Pouthika, G. Madhumitha, Design and development of Carissa edulis fruit extract mediated bimetallic CuO-NiO-HNT composites for photocatalytic removal of food dye and antibiotic drug, J. Mol. Struct. 1295 (2024) 136665, https://doi.org/10.1016/j.molstruc.2023.136665.
[45] S. Cathrin Lims, S. Divya, M. Jose, Design of CuO @ SiO_2 core shell nanocomposites and its applications to photocatalytic degradation of Rhodamine B dye, Opt. Mater. 144 (2023) 114356, https://doi.org/10.1016/j.optmat.2023.114356.
[46] M.B. Mobarak, H. Md Sahadat, F. Chowdhury, S. Ahmed, Synthesis and characterization of CuO nanoparticles utilizing waste fish scale and exploitation of XRD peak profile analysis for approximating the structural parameters, Arab. J. Chem. 15 (10) (2022) 104117, https://doi.org/10.1016/j.arabjc.2022.104117.
[47] C. Chuaicham, J. Trakulmututa, K. Shu, S. Shenoy, A. Srikhaow, L. Zhang, S. Mohan, K. Sekar, K. Sasaki, Recent clay-based photocatalysts for wastewater treatment, Separations 10 (2023) 77, https://doi.org/10.3390/separations10020077.
[48] K. Velsankar, R.M.A. A.K, R. Preethi, V. Muthulakshmi, S. Sudhahar, Green synthesis of CuO nanoparticles via *Allium sativum* extract and its characterizations on antimicrobial, antioxidant, antilarvicidal activities, J. Environ. Chem. Eng. 8 (2020) 104123, https://doi.org/10.1016/j.jece.2020.104123.
[49] M. Qiu, L. Liu, Q. Ling, Y. Cai, S. Yu, S. Wang, D. Fu, B. Hu, X. Wang, Biochar for the removal of contaminants from soil and water: a review, Biochar 4 (1) (2022) 19, https://doi.org/10.1007/s42773-022-00146-1.
[50] S.E. Safitri, Y. Yulizar, Facile green preparation of Y_2O_3 decorated with $ZnFe_2O_4$ using citrus limon (L.) osbeck leaf extract for photocatalytic degradation of malachite green, Appl. Surf. Sci. 21 (2024) 1000589, https://doi.org/10.1016/j.apsadv.2024.100589.
[51] M. Movahedi, A.R. Mahjoub, S. Janitabar-Darzi, Photodegradation of Congo red in aqueous solution on ZnO as an alternative catalyst to TiO_2, J. Iran. Chem. Soc. 6 (3) (2009) 570–577, https://doi.org/10.1007/BF03246536.

[52] R. Raliya, C. Avery, S. Chakrabarti, P. Biswas, Photocatalytic degradation of methyl orange dye by pristine titanium dioxide, zinc oxide, and graphene oxide nanostructures and their composites under visible light irradiation, Appl. Nanosci. 7 (2017) 253–259, https://doi.org/10.1007/s13204-017-0565-z.
[53] F.X. Deng, E. Brillas, Advances in the decontamination of wastewaters with synthetic organic dyes by electrochemical Fenton-based processes, Sep. Purif. Technol. 316 (2023) 123764, https://doi.org/10.1016/-j.seppur.2023.123764.
[54] C. Yang, W. Dong, G. Cui, Y. Zhao, X. Shi, X. Xia, B. Tang, W. Wang, Highly efficient photocatalytic degradation of methylene blue by P2ABSA-modified TiO_2 nanocomposite due to the photosensitization synergetic effect of TiO_2 and P_2ABSA, RSC Adv. 7 (2017) 23699–23708, https://doi.org/10.1039/C7RA02423A.
[55] A.M. El-Khawaga, D.S.R. Khafaga, Y.A. Fahim, A.M. Fadl, Harnessing copper oxide nanoparticles for advanced photocatalytic, antimicrobial, and larvicidal applications, Sci. Rep. 15 (2025) 40369, https://doi.org/10.1038/s41598-025-25441-2.
[56] X. Gu, S. Lin, K. Qi, Y. Yan, R. Li, V. Popkov, O. Almjasheva, Application of tungsten oxide and its composites in photocatalysis, Sep. Purif. Technol. 345 (2024) 127299, https://doi.org/10.1016/j.seppur.2024.127299.
[57] W.K. Jo, R.J. Tayade, New generation energy-efficient light source for photocatalysis: LEDs for environmental applications, Ind. Eng. Chem. Res. 53 (2014) 2073–2084, https://doi.org/10.1021/ie404176g.
[58] C.S. Philip, A. Nivetha, C. Sakthivel, C.G. Veena, I. Prabha, Novel fabrication of cellulose sprinkled crystalline nanocomposites using economical fibrous sources: high performance, compatible catalytic and electrochemical properties, Microporous Mesoporous Mater. 318 (2021) 111021, https://doi.org/10.1016/j.micromeso.2021.111021.
[59] N. Barsan, U. Weimar, Conduction model of metal oxide gas sensors, J. Electroceram. 7 (2001) 143–167, https://doi.org/10.1023/A:1014405811371.
[60] M. Nazim, A.A.P. Khan, A.M. Asiri, J.H. Kim, Exploring rapid photocatalytic degradation of organic pollutants with porous CuO nanosheets: synthesis, dye removal, and kinetic studies at room temperature, ACS Omega 6 (2021) 2601–2612, https://doi.org/10.1021/acsomega.0c04747.